

Structure and mechanogating mechanism of the Piezo1 channel

Qiancheng Zhao^{1,2,3*}, Heng Zhou^{1,2*}, Shaopeng Chi^{1,2,3*}, Yanfeng Wang^{1,2,3*}, Jianhua Wang⁴, Jie Geng^{1,2,3}, Kun Wu^{1,2,3}, Wenhao Liu^{1,2,3,5}, Tingxin Zhang^{1,2,3,5}, Meng-Qiu Dong⁴, Jiawei Wang¹, Xueming Li^{1,2} & Bailong Xiao^{1,2,3}

The mechanosensitive Piezo channels function as key eukaryotic mechanotransducers. However, their structures and mechanogating mechanisms remain unknown. Here we determine the three-bladed, propeller-like electron cryo-microscopy structure of mouse Piezo1 and functionally reveal its mechanotransduction components. Despite the lack of sequence repetition, we identify nine repetitive units consisting of four transmembrane helices each—which we term transmembrane helical units (THUs)—which assemble into a highly curved blade-like structure. The last transmembrane helix encloses a hydrophobic pore, followed by three intracellular fenestration sites and side portals that contain pore-property-determining residues. The central region forms a 90 Å-long intracellular beam-like structure, which undergoes a lever-like motion to connect THUs to the pore via the interfaces of the C-terminal domain, the anchor-resembling domain and the outer helix. Deleting extracellular loops in the distal THUs or mutating single residues in the beam impairs the mechanical activation of Piezo1. Overall, Piezo1 possesses a unique 38-transmembrane-helix topology and designated mechanotransduction components, which enable a lever-like mechanogating mechanism.

The evolutionarily conserved Piezo proteins, including Piezo1 and Piezo2, have been established as the long-sought-after mechanosensitive cation channels in mammals^{1–4}. Piezo channels have crucial roles in various mechanotransduction processes^{5,6}. For example, Piezo1 expressed in blood vessels is crucial for sensing blood-flow-associated shear stress for proper blood vessel development^{7,8}, whereas Piezo2 mediates touch^{9–12}, proprioception¹³, airway stretching and lung inflation¹⁴. Furthermore, mutations in Piezo genes have been linked to several hereditary human diseases that involve mechanotransduction¹⁵.

Piezo proteins represent a distinct class of membrane proteins with numerous transmembrane (TM) helices^{1,16}. The full-length 2,547-residue mouse Piezo1 heterologously expressed in HEK293T cells and purified² has been shown to mediate mechanosensitive cation currents when reconstituted into lipid bilayers^{2,17}, demonstrating its ability to form intrinsically mechanosensitive cation channels. In cells, Piezo channels can respond to various forms of mechanical stimulation, including poking, stretching and shear stress^{1,8,18}.

A medium-resolution cryo-electron microscopy (cryo-EM) structure of mouse Piezo1 has been previously determined, revealing its three-bladed, propeller-shaped trimeric architecture³. Combining structural and functional characterizations, we have proposed that the complex mouse Piezo1 might be divided into the central ion-conducting pore module and the peripheral blade-like mechanotransduction modules^{3,4,19}. However, only 14 apparent TM helices in each subunit were resolved, and an alanine model of 492 residues together with 227 residues of the C-terminal extracellular domain (CED) resolved by X-ray crystallization was built³. Thus, we set up to determine high-resolution structures of Piezo1 and to functionally reveal its key mechanotransduction components.

Structure determination of mouse Piezo1

On the basis of the analysis of 10,171 micrographs with approximately 2.8 million particles, we determined a structure of mouse Piezo1 to an

overall resolution of 3.97 Å (Extended Data Figs 1 and 2, Supplementary Fig. 1 and Supplementary Table 1). Overall, the central region including the intracellular beam and the TM region, which contains the 14 TM helices resolved in the previously determined structure³, has clearly better resolution (3–4 Å) than the distal blades and the central cap (4–7 Å). We identified 12 additional TM helices that reside in the distal blade (Fig. 1b), which became better resolved when the peripheral blades were subjected to local refinement (Extended Data Figs 2 and 3a). The connections between the N and C termini of the CED and the outer and inner helices (OH and IH, respectively) were also better resolved after local refinement (Extended Data Figs 2 and 3b), allowing assignment of the OH and IH from each subunit. We built and refined a structure model for Piezo1, which supports important assignments to the major structural domains as shown in Fig. 2, Extended Data Fig. 4 and Supplementary Fig. 1. Consistent with the previous structure³, mouse Piezo1 possesses a three-bladed, propeller-shaped architecture that comprises the central cap, three peripheral blades and three long intracellular beams (Fig. 1a). The diameter from the top view and the axial height of the structure are 185 Å and 140 Å, respectively (Fig. 1a, middle).

The unusually curved peripheral TM blade

The 24 peripheral TM helices in each subunit are organized into 12 parallel pairs (Fig. 2a), extending from the central OH–IH pair to the periphery in a highly curved configuration (Figs 1b and 2a). When viewed perpendicularly to the plasma membrane plane, each TM blade twists in a clockwise manner to form a half-circled superhelical structure, resembling the blade of a typical propeller (Fig. 1). The proximal TM25–TM36 and peripheral TM13–TM24 seem to segregate into two TM segments, which form a 100° angle (Fig. 1b, left). Notably, when viewed parallel to the plasma membrane plane, the peripheral TM13–TM24 form a 140° angle relative to the proximal TM25–TM36 (Fig. 1b, middle), which might reside in the normal plasma membrane plane.

¹School of Pharmaceutical Sciences or Life Sciences, Tsinghua University, Beijing 100084, China. ²Tsinghua-Peking Joint Center for Life Sciences, Tsinghua University, Beijing 100084, China. ³IDG/McGovern Institute for Brain Research, Tsinghua University, Beijing 100084, China. ⁴National Institute of Biological Sciences, Beijing 102206, China. ⁵Joint Graduate Program of Peking-Tsinghua-NIBS, School of Life Sciences, Tsinghua University, Beijing 100084, China.

*These authors contributed equally to this work.

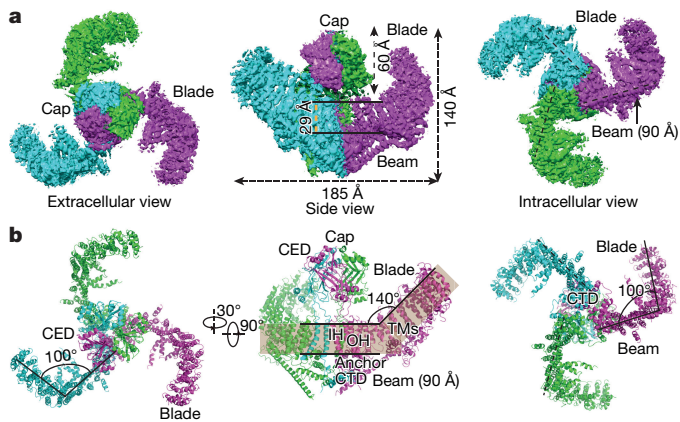


Figure 1 | Overall structure of mouse Piezo1. **a**, The indicated view of the sharpened map (6σ contour level) filtered to a resolution of 3.97 Å, with each subunit colour-coded and the major domains labelled. **b**, Cartoon models with each subunit colour-coded. In the middle panel, the peripheral blade of the front subunit is omitted for a better view of the curvature of the TM helices. The shadow area indicates a planar and a potentially curved membrane plane where TM helices reside.

Such an organization seems to place TM25–TM36 in a normal plane, but TM13–TM24 in a highly curved membrane plane. However, it remains possible that the curved organization of the TM helices might be due to removal of the purified Piezo1 proteins from the membrane. Characteristically, TM13, TM17, TM21, TM25 and TM29 form L-shaped helical structures with one or two preceding short helices, namely TM13^{pre α 1}, TM17^{pre α 1}, TM21^{pre α 2}, TM25^{pre α 2} and TM29^{pre α 2}, respectively, which are positioned parallel to the membrane and collectively form an intracellular helical layer immediately underneath the membrane (Fig. 2a and Extended Data Fig. 3a), which might help to stabilize the curved TM blade in the membrane. The highly curved TM blade and the intracellular helical layer might represent unique structural features not only for mechanosensing and transduction but also for inducing local membrane curvature.

The THU repeats and a 38-TM topology model

The assignment of residues into the peripheral TM25–TM36 revealed three repetitive folds containing four TM helices each, which we term THUs (Fig. 2 and Extended Data Figs 4, 5). Within each THU, the first two TM helices, closely spaced with a short extracellular linker, are folded towards the central end (referring to the OH–IH pair) of the TM blade. The second TM helix folds backward to the distal end and connects to the third TM helix, which connects to the fourth TM through an extracellular linker of 30–50 residues. Two consecutive THUs are connected through a relatively long intracellular loop, which spans all eight TM helices and consequently arranges the four pairs of TM helices in series (Fig. 2). TM25–TM28, TM29–TM32 and TM33–TM36 form THU7, THU8 and THU9, respectively (Fig. 2). The loop that links TM27 and TM28 was experimentally confirmed to be located extracellularly (Extended Data Fig. 6).

On the basis of the folding characteristics of the THUs, topology and secondary structure prediction, and cross-linking results (Extended Data Figs 4, 5, 7 and Supplementary Fig. 1), the structurally revealed TM13–TM16, TM17–TM20 and TM21–TM24 helices were assigned to THU4, THU5 and THU6, respectively. These six tandem THUs constitute the highly curved TM blade (Fig. 2). Many topology prediction programs have predicted 12 TM helices in the unresolved N-terminal region of approximately 500 residues (Extended Data Fig. 5). Each 4-TM bundle of the predicted 12 TM helices follows the typical folding features of the THU. In line with the prediction, the second extracellular loops in each THU have been experimentally verified to be located extracellularly²⁰ (Fig. 2b). Furthermore, we identified residues from the linkers of TM4–TM5 (THU1–THU2), TM8–TM9

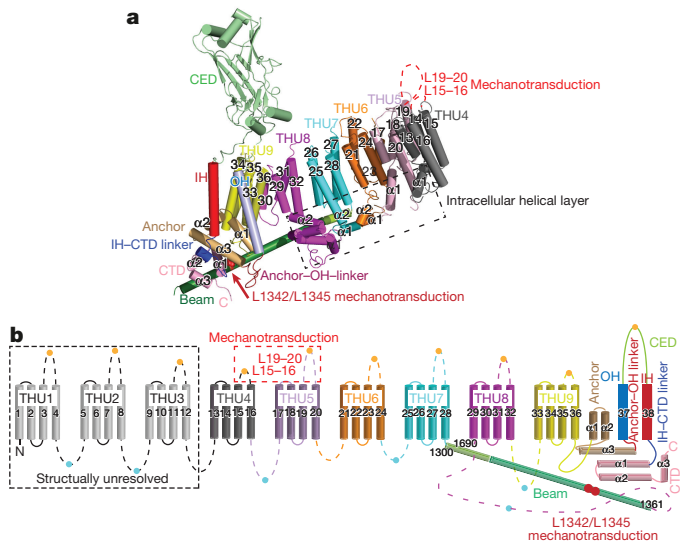


Figure 2 | Repetitive THUs and a 38-TM topology model. **a**, Cartoon model showing cylindrical helices displays one subunit, with individual THUs and major structural domains labelled. The functionally characterized extracellular loops of TM15–TM16 (L15–16) and TM19–TM20 (L19–20) are shown in red dashed lines, and residues L1342 and L1345 in the beam are shown by red spheres. **b**, A 38-TM topology model, colour-coded to match the cartoon models in **a**. Some intracellular helices shown in **a** are omitted for better illustration of the THUs and beam features. Yellow dots mark the experimentally verified extracellular loops, and blue dots indicate loops that can be cross-linked to residues in the intracellular loops of TM28–TM29 and TM32–TM33.

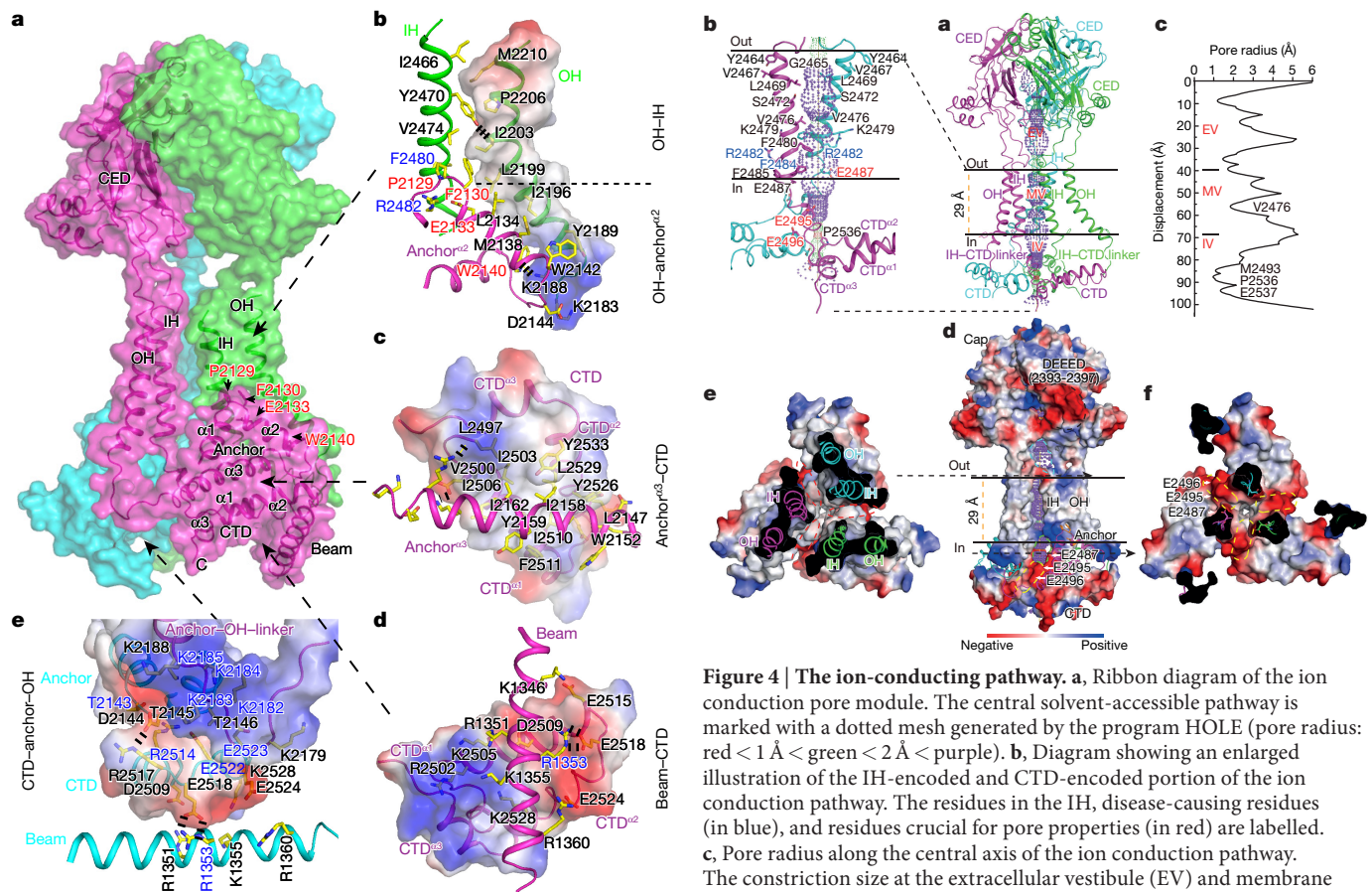
(THU2–THU3), TM16–TM17 (THU4–THU5) that cross-linked with residues in the intracellular loop of TM28–TM29 (THU7–THU8) or TM32–TM33 (THU8–THU9) (Extended Data Fig. 7 and Fig. 2b), indicating the intracellular localization of these loops. Based on these lines of evidence, we assign the N-terminal 12 TM helices to THU1–THU3. Therefore, the peripheral 36 TM helices are folded into nine tandem repetitive THUs to form the unique TM blade. Together with the OH and IH, Piezo1 might possess an unprecedented 38-TM topology with a total of 114 TM helices in the trimeric channel complex.

The intracellular beam

Three characteristic long density rods roughly 90 Å in length are exposed on the intracellular surface of THU7–THU9 and the C-terminal domain (CTD), and are termed the beams (Figs 1, 2). We were able to assign H1300–S1362 to the beam, which is apparently kinked at residues A1316 and S1317 (Extended Data Fig. 4). This assignment is in line with the predicted continuous long helix immediately following TM28 (Supplementary Fig. 1) and supported by the mass spectrometry for cross-linked peptides (CXMS) results (Extended Data Fig. 7). The THU7–THU8 loop is the largest intracellular loop of Piezo1, containing approximately 390 residues. According to the structure, this loop starts at the distal end of the beam, extends 90 Å into the centre of the complex to interact with the CTD, and then folds back to the distal end of the beam before connecting to TM29 (Fig. 2). The organization of this loop might render the beam an ideal structure for mechanical transmission from the distal THUs to the central ion-conducting pore.

The beam–CTD–anchor–IH/OH relaying interfaces

CTD ^{α 1–3}, consisting of the three α -helices α 1, α 2 and α 3, forms a triangular plane parallel to the plasma membrane, positioned immediately above the proximal end of the beam (Figs 2a and 3a). The beam-facing side of the triangular CTD plane is clearly separated into two surfaces with negative and positive electrostatic potentials (Fig. 3d). The beam



crosses through the boundary of the two surfaces, forming interactions with both CTD^{α1} and CTD^{α2}. The disease-associated residue R1353 might form a salt bridge with E2518 (Fig. 3d, e).

The anchor domain, uniquely positioned between the OH–IH pair and the CTD plane, results in a swap of the OH–CED–IH into the neighbouring subunit (Figs 1 and 3a). Anchor^{α1–2} forms an inverted v-shaped structure that penetrates into the inner leaflet of the membrane, containing the evolutionarily conserved motif among Piezo homologues, P2129–F2130(X2)–E2133(X6)–W2140²¹. P2129, F2130 and E2133 are in close proximity to the intracellular end of the pore-lining IH (Fig. 3a, b), which may stabilize the integrity of the ion-conducting pore. Indeed, although E2133 is not located in the ion-conducting pathway, its mutations affect the pore properties²⁰. Anchor^{α2} lies parallel to the inner portion of the OH, which is kinked at residue I2203, forming hydrophobic interactions (Fig. 3a, b). The upper portion of the OH above the kink lies parallel to the IH and also forms extensive hydrophobic interactions (Fig. 3a, b). Thus, the OH might help to stabilize the IH-encompassing pore.

The long anchor^{α3}, in parallel with the membrane plane, forms a hydrophobic interface with the CTD (Fig. 3a, c). It connects to the OH through the lysine-rich anchor–OH–linker (2173–KKYPQPKGQK—2185), which forms a tripartite interaction with the polar residue-rich anchor^{α2–3} turn (2143–TDTTSL–2148), and the glutamate-rich region of the CTD (2514–RETRELEEEE–2524) (Fig. 3a, e). Several residues, including T2143, 2182–KKKK–2185,

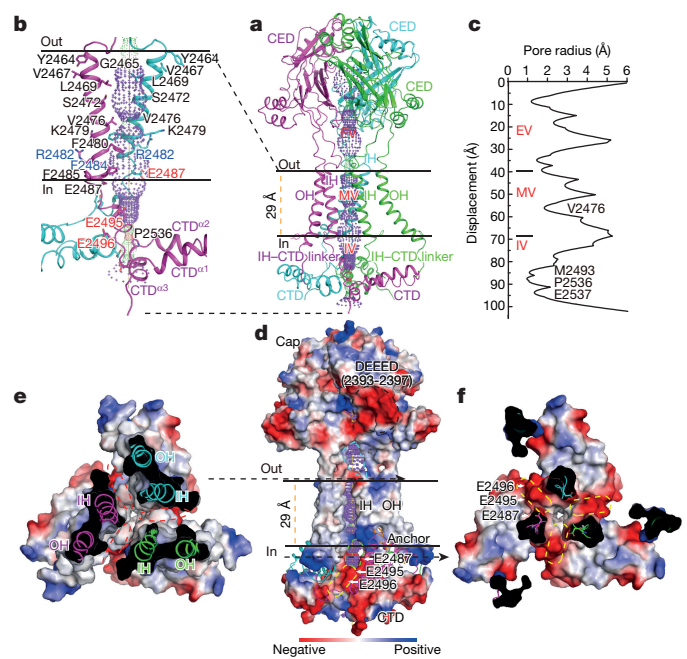


Figure 4 | The ion-conducting pathway. **a**, Ribbon diagram of the ion conduction pore module. The central solvent-accessible pathway is marked with a dotted mesh generated by the program HOLE (pore radius: red < 1 Å < green < 2 Å < purple). **b**, Diagram showing an enlarged illustration of the IH-encoded and CTD-encoded portion of the ion conduction pathway. The residues in the IH, disease-causing residues (in blue), and residues crucial for pore properties (in red) are labelled. **c**, Pore radius along the central axis of the ion conduction pathway. The constriction size at the extracellular vestibule (EV) and membrane vestibule (MV) junction is based on an alanine model of the CED–IH linker. IV, intracellular vestibule. **d**, Pore module showing the surface electrostatic potential. The central pathway is marked with a dotted mesh, showing the opening to the membrane. The extracellular and intracellular fenestration sites open to the extracellular vestibule and the intracellular vestibule are marked by cyan and green dashed lines, respectively. The intracellular side portals are marked with the yellow dashed lines. **e**, Diagram showing a cross-section at the arrow indicated plane, showing the hydrophobic transmembrane pore and the side openings to the membrane marked by the dashed red ovals. **f**, Diagram showing a cross-section near the E2487 residue, highlighting the three side portals formed by E2487, E2495 and E2496.

R2514, E2522 and E2523, are associated with disease. Furthermore, we have found that the anchor–OH–linker is important not only for mechanogating but also for mediating the interaction with the sarco/endoplasmic reticulum Ca²⁺ ATPase (SERCA) and the resulting inhibition of Piezo1²².

The ion-conducting pathway

The OH–CED–IH–CTD structure trimerizes to form the well-resolved central pore module^{3,4}. Subjecting the structure of the pore module to the online PPM server²³ revealed that the entire IH spanning from Y2464 to F2485 defines the transmembrane region of approximately 29 Å thick (Fig. 4a, b). The central solvent-accessible pathway can be separated into the extracellular vestibule above the membrane, the membrane vestibule within the membrane and the intracellular vestibule immediately below the membrane (Fig. 4a, c). The IH lacks negatively charged residues and encloses a hydrophobic transmembrane pore with pore-facing residues shown in Fig. 4a, b, e. V2476 forms a constriction point in the middle of the membrane vestibule (Fig. 4a–c). Notably, the transmembrane pore is not completely sealed from the membrane by the three IHs (Fig. 4d, e). Two neighbouring IHs and one OH form a hydrophobic groove open to the transmembrane pore (Fig. 4d, e). This feature raises an intriguing possibility that membrane lipids may affect the ion permeation and gating of Piezo1.

Although the top of the extracellular vestibule is sealed and the bottom end of the intracellular vestibule is constricted (Fig. 4a, c), both vestibules have large fenestration sites immediately above and below the membrane, respectively (Fig. 4d). The patch of negatively charged residues 2393-DEEED-2397, located right above the extracellular fenestration sites (Fig. 4d), has a crucial role in controlling efficient ion conduction and the selection of cations over anions^{3,4}. These features suggest that cations might enter the ion-conducting pathway through the extracellular fenestration sites. The intracellular fenestration sites have a size of roughly $10 \times 15 \text{ \AA}$, through which the intracellular vestibule connects to three $\sim 8\text{-\AA}$ -wide side portals with negative electrostatic potentials, comprising E2487 from one subunit and E2495 and E2496 from a neighbouring subunit (Fig. 4d, f). Mutating these residues affects the unitary conductance, Ca^{2+} permeability and ruthenium red responsiveness of mouse Piezo1⁴. Given that E2495 and E2496 are not located along the central pore axis but rather on the side portals (Fig. 4d, f), we propose that the three intracellular fenestration sites and the connecting side portals might represent the intracellular cation permeation pathways. Nevertheless, it remains to be determined whether the top seal of the extracellular vestibule and the bottom constriction site of the intracellular vestibule might be gated to allow ion conduction. Previous studies have indicated that the diameter of the ion-conducting pathway upon opening is larger than 8 \AA ²⁴. Thus, the observed constriction sites in the transmembrane pore indicate that the structure represents a closed conformation (Fig. 4a, c).

Motion features of Piezo1

Comparing the nine distinct structures derived from symmetry-free classification revealed conformational changes at the peripheral blades, the beam and the cap (Extended Data Fig. 8). Notably, as shown in Fig. 5a, each subunit within the trimeric complex might be able to move independently. This independent motion of the individual subunit might be functionally relevant, as a given force in the membrane is unlikely to be evenly distributed among the three subunits unless the force directly acts on the central cap region. We further compared two structures of 4.51 \AA and 4.40 \AA resolution, resulting from class 3 and class 6 of the 9 classified structures with C3 symmetry, respectively (Extended Data Fig. 2). Superimposition of the two maps shows that the IHs, anchor and CTD were nearly unchanged (Fig. 5c, d). By contrast, the cap of class 6 rotates in a clockwise manner relative to that of class 3 (Fig. 5b). The TM blades of class 6 undergo an anticlockwise twist, with a graded decrease in motion from the distal THU4 to the proximal THU9 (Fig. 5b). The intracellular helical layer exhibits a vertical motion (Fig. 5d), which might flatten the curved distal blades and the residing membrane. Notably, the beam displays uneven movement with large motion at the distal beam while subtle movement at the proximal end (Fig. 5d–f). As a whole, the motion feature of the peripheral TM helices and the beams is reminiscent of a lever apparatus (Fig. 5f). We next carried out biochemical and functional studies to test the importance of the distal blade and the beam in the mechanical activation of Piezo1.

Extracellular loops are crucial for mechanical activation

We generated a series of deletion mutants in which the extracellular loops of distal THU1–THU6 were deleted (replaced with a short poly-glycine GGGGG linker) one at a time (Fig. 2b). Among the deletion mutants, only $\Delta\text{L15–16}$ and $\Delta\text{L19–20}$ had comparable expression to that of wild-type mouse Piezo1 (Extended Data Fig. 9d and Supplementary Fig. 2b), and were properly targeted to the plasma membrane (Extended Data Fig. 9a–c and Supplementary Fig. 2a). Together, these data suggest that the loop regions of TM3–TM4, TM7–TM8, TM11–TM12 and TM23–TM24 are crucial for the proper expression and plasma membrane targeting of Piezo1. $\Delta\text{L15–16}$ and $\Delta\text{L19–20}$, but not other mutants, were functional (Fig. 6a, b). However, the poking-induced maximal whole-cell currents (I_{max}) of $\Delta\text{L15–16}$ and $\Delta\text{L19–20}$ were only $4.3 \pm 1.3\%$ (mean \pm s.e.m.) and $3.3 \pm 0.8\%$ of the Piezo1-mediated

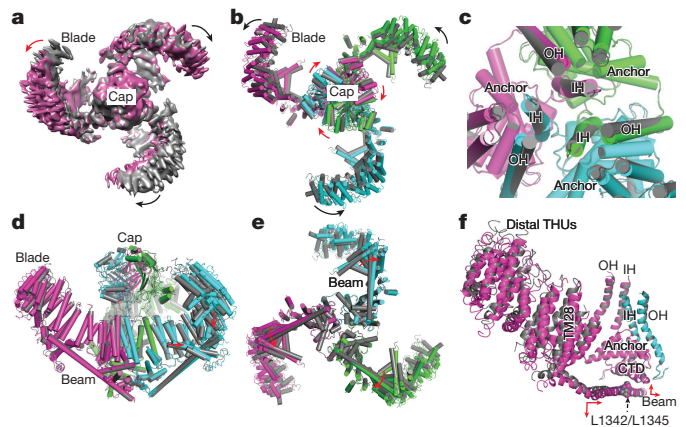


Figure 5 | Motion features. **a**, Overlay of the class 4 (grey) and class 6 (purple) structures without symmetry, showing the opposite twisting motion of one blade (marked by the red arrow) compared to the other two blades (marked by black arrows). **b**, **d**, **e** The indicated view of the superimposed class 3 (grey) and class 6 (colour-coded) structures with C3 symmetry. **c**, Diagram showing the enlarged top view of the pore by omitting the cap from **b**. **f**, Diagram showing the uneven motion of the beam. The L1342 and L1345 residues are shown in sphere representation. The distal THUs and the central CTD–anchor–OH/IH relaying interfaces are included to illustrate the lever-like mechanotransduction apparatus constituted by the beam.

current, respectively (Fig. 6a, b). Similar results were observed in $\Delta\text{L15–16}$ - or $\Delta\text{L19–20}$ -transfected Piezo1-knockout HEK293 cells in which the endogenous *Piezo1* gene was disrupted²⁵ (Extended Data Fig. 9e). Furthermore, the stretching-induced Piezo1-like currents were abolished in cells expressing the two mutants (Fig. 6d, e). Yoda1, a chemical agonist of Piezo1, can evoke Piezo1-dependent Ca^{2+} responses and potentiate Piezo1-mediated mechanical currents²⁶. Compared to Piezo1, the two mutants showed comparable Yoda1-induced fold changes of the poking-evoked currents (Fig. 6c) and Ca^{2+} responses (Fig. 6f and Extended Data Fig. 9i), suggesting that the two mutants retain normal Yoda1 responsiveness. In line with their drastically reduced mechanically evoked currents in the absence of Yoda1 (Fig. 6a, b), the poking-induced I_{max} of the two mutants was also smaller than that of Piezo1 when Yoda1 was present (Fig. 6a and Extended Data Fig. 9f). The inactivation kinetics of the two mutants was similar to that of Piezo1 (Extended Data Fig. 9g, h), suggesting that deleting the two loops does not affect the inactivation process. Together, these data demonstrate that the two extracellular loops have a crucial role in the mechanical activation of Piezo1.

L1342 and L1345 are required for mechanical activation

Deleting the residues from 1280 to 1360 that contain the beam structure abolished the expression of the resulting mutant protein (Extended Data Fig. 9d), in line with the structural importance of the beam. Interestingly, the beam domain contains a predicted coiled-coil motif, 1342-LAQLKRQM-1349, which is located in the proximal end of the beam near the CTD and seems to be stable (Fig. 5f). The L1342A/L1345A double mutant was properly expressed in the plasma membrane (Extended Data Fig. 10a, b). However, the mutant exhibited reduced poking-induced currents (Fig. 6g, h). Its I_{max} reached only approximately 21% of the Piezo1-mediated current (Fig. 6h). L1342A/L1345A also exhibited reduced stretching-induced current (47% of the Piezo1 current) (Fig. 6i), a rightward shifted pressure–current relationship (Fig. 6j), and enhanced the pressure required to activate half of the channel (P_{50}) (Piezo1 versus L1342A/L1345A: -27.1 ± 3.1 versus $-46.2 \pm 6.4 \text{ mm Hg}$) (Fig. 6k). The single-channel conductance (Extended Data Fig. 10c–e) of the mutant was not affected. Furthermore, neither mutating the residue Q1344 (Extended Data Fig. 10f) nor mutating residues in close proximity to L1342 and L1345, including T2103 and R2104 in the TM36 anchor–linker and L2512 and T2516

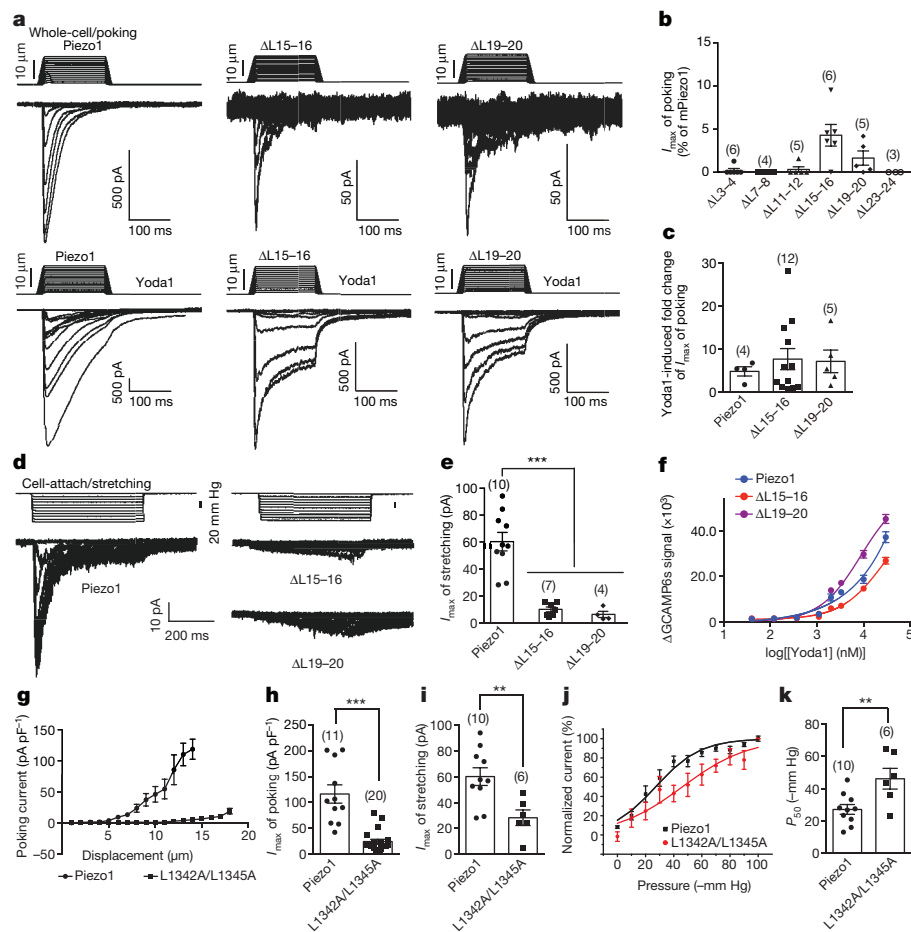


Figure 6 | Regions and residues critical for the mechanical activation of Piezo1. **a**, Representative traces of poking-induced inward currents at -60 mV in the whole-cell configuration in the absence or presence of $30 \mu\text{M}$ Yoda1. **b**, Scatter plot of the maximal poking-induced currents of the indicated mutants normalized to the Piezo1 current. **c**, Yoda1-induced fold changes of the poking-induced I_{max} . **d**, Representative stretching-activated currents at -80 mV. **e**, Scatter plot of the maximal stretching-induced currents. $***P < 0.0001$, one-way ANOVA with Dunn's multiple comparison test. **f**, Yoda1 dose response curves of the indicated constructs assayed using a fluorescent imaging plate reader (FLIPR). The curves were fitted with a Boltzmann equation. $n = 4$ wells. **g**, Relationship between

in the CTD (Extended Data Fig. 10g, h), affected the poking-induced currents. Collectively, these data suggest that L1342 and L1345 are specifically required for the mechanogating of Piezo1.

The $\Delta\text{L15-16}$ and $\Delta\text{L19-20}$ mutants completely lost their ability to generate stretch-induced currents (Fig. 6d, e), but could produce residual poking-currents (Fig. 6a, b). The L1342A/L1345A mutant has more markedly reduced poking-induced currents than stretching-induced currents (Fig. 6h, i). These observations suggest that different forms of mechanical stimulation may use discrete molecular bases of Piezo1 for mechanotransduction.

Discussion

Piezo channels serve as a principal type of mechanotransduction channels. Here, via determining the mouse Piezo1 structures, we have revealed its unique topological features, the ion-conducting pathway, and the lever-like motion of the blade-beam. Functionally, we have identified regions and single residues that are crucial for the mechanical activation of Piezo1. We propose that Piezo1 might use its characteristically curved blades and the long beams with L1342 and L1345 as a pivot to form a lever-like apparatus. Such a lever-like mechanotransduction mechanism might enable Piezo channels to effectively convert a large

poking-induced currents and the applied poking displacement. **h**, Scatter plot of the maximal poking-induced currents recorded at -60 mV. $***P < 0.0001$, unpaired, two tailed Student's t -test. **i**, Scatter plot of the maximal stretching-induced currents. $**P = 0.0045$ unpaired, two tailed Student's t -test. **j**, Pressure-current relationships of the stretching-induced currents. The curves were fitted with a Boltzmann equation. **k**, Scatter plot of the P_{50} calculated from the fit of the pressure-current relationship of individual recordings with a Boltzmann equation. $**P = 0.0091$, unpaired, two tailed Student's t -test. The number of recorded cells is shown above the bar. All data are mean \pm s.e.m.

conformational change of the distal blades to a relatively slight opening of the central pore, allowing cation-selective permeation. Three sets of such lever-like apparatus are further assembled into a gigantic propeller-like machinery, which might confer a coordinated mechanosensitivity. Thus, different classes of mechanosensitive ion channels, such as the bacterial mechanosensitive channels with large conductance (MscL), the mechanosensitive K2P channels and the NOMPC mechanotransduction channels, use distinct structural and functional mechanisms for mechanotransduction^{27–29}.

Online Content Methods, along with any additional Extended Data display items and Source Data, are available in the online version of the paper; references unique to these sections appear only in the online paper.

Received 24 October 2017; accepted 12 January 2018.

Published online 22 January 2018.

- Coste, B. *et al.* Piezo1 and Piezo2 are essential components of distinct mechanically activated cation channels. *Science* **330**, 55–60 (2010).
- Coste, B. *et al.* Piezo proteins are pore-forming subunits of mechanically activated channels. *Nature* **483**, 176–181 (2012).
- Ge, J. *et al.* Architecture of the mammalian mechanosensitive Piezo1 channel. *Nature* **527**, 64–69 (2015).

4. Zhao, Q. *et al.* Ion permeation and mechanotransduction mechanisms of mechanosensitive Piezo channels. *Neuron* **89**, 1248–1263 (2016).
5. Geng, J., Zhao, Q., Zhang, T. & Xiao, B. In touch with the mechanosensitive Piezo channels: structure, ion permeation, and mechanotransduction. *Curr. Top. Membr.* **79**, 159–195 (2017).
6. Ranade, S. S., Syeda, R. & Patapoutian, A. Mechanically activated ion channels. *Neuron* **87**, 1162–1179 (2015).
7. Ranade, S. S. *et al.* Piezo1, a mechanically activated ion channel, is required for vascular development in mice. *Proc. Natl Acad. Sci. USA* **111**, 10347–10352 (2014).
8. Li, J. *et al.* Piezo1 integration of vascular architecture with physiological force. *Nature* **515**, 279–282 (2014).
9. Maksimovic, S. *et al.* Epidermal Merkel cells are mechanosensory cells that tune mammalian touch receptors. *Nature* **509**, 617–621 (2014).
10. Woo, S. H. *et al.* Piezo2 is required for Merkel-cell mechanotransduction. *Nature* **509**, 622–626 (2014).
11. Ranade, S. S. *et al.* Piezo2 is the major transducer of mechanical forces for touch sensation in mice. *Nature* **516**, 121–125 (2014).
12. Ikeda, R. *et al.* Merkel cells transduce and encode tactile stimuli to drive A β -afferent impulses. *Cell* **157**, 664–675 (2014).
13. Woo, S. H. *et al.* Piezo2 is the principal mechanotransduction channel for proprioception. *Nat. Neurosci.* **18**, 1756–1762 (2015).
14. Nonomura, K. *et al.* Piezo2 senses airway stretch and mediates lung inflation-induced apnoea. *Nature* **541**, 176–181 (2017).
15. Alper, S. L. Genetic diseases of PIEZO1 and PIEZO2 dysfunction. *Curr. Top. Membr.* **79**, 97–134 (2017).
16. Kamajaya, A., Kaiser, J. T., Lee, J., Reid, M. & Rees, D. C. The structure of a conserved Piezo channel domain reveals a topologically distinct β sandwich fold. *Structure* **22**, 1520–1527 (2014).
17. Syeda, R. *et al.* Piezo1 channels are inherently mechanosensitive. *Cell Rep.* **17**, 1739–1746 (2016).
18. Cox, C. D. *et al.* Removal of the mechanoprotective influence of the cytoskeleton reveals PIEZO1 is gated by bilayer tension. *Nat. Commun.* **7**, 10366 (2016).
19. Wang, Y. & Xiao, B. The mechanosensitive Piezo1 channel: structural features and molecular bases underlying its ion permeation and mechanotransduction. *J. Physiol. (Lond.)* (2017).
20. Coste, B. *et al.* Piezo1 ion channel pore properties are dictated by C-terminal region. *Nat. Commun.* **6**, 7223 (2015).
21. Prole, D. L. & Taylor, C. W. Identification and analysis of putative homologues of mechanosensitive channels in pathogenic protozoa. *PLoS ONE* **8**, e66068 (2013).
22. Zhang, T., Chi, S., Jiang, F., Zhao, Q. & Xiao, B. A protein interaction mechanism for suppressing the mechanosensitive Piezo channels. *Nat. Commun.* **8**, 1797 (2017).
23. Lomize, M. A., Pogozheva, I. D., Joo, H., Mosberg, H. I. & Lomize, A. L. OPM database and PPM web server: resources for positioning of proteins in membranes. *Nucleic Acids Res.* **40**, D370–D376 (2012).
24. Gnanasambandam, R., Bae, C., Gottlieb, P. A. & Sachs, F. Ionic selectivity and permeation properties of human PIEZO1 channels. *PLoS ONE* **10**, e0125503 (2015).
25. Lukacs, V. *et al.* Impaired PIEZO1 function in patients with a novel autosomal recessive congenital lymphatic dysplasia. *Nat. Commun.* **6**, 8329 (2015).
26. Syeda, R. *et al.* Chemical activation of the mechanotransduction channel Piezo1. *eLife* **4**, (2015).
27. Chang, G., Spencer, R. H., Lee, A. T., Barclay, M. T. & Rees, D. C. Structure of the MscL homolog from *Mycobacterium tuberculosis*: a gated mechanosensitive ion channel. *Science* **282**, 2220–2226 (1998).
28. Brohawn, S. G., Campbell, E. B. & MacKinnon, R. Physical mechanism for gating and mechanosensitivity of the human TRAAK K⁺ channel. *Nature* **516**, 126–130 (2014).
29. Jin, P. *et al.* Electron cryo-microscopy structure of the mechanotransduction channel NOMPC. *Nature* **547**, 118–122 (2017).

Supplementary Information is available in the online version of the paper.

Acknowledgements We thank N. Yan for critical discussion, and the Beijing Advanced Innovation Center for Structural Biology for facility and financial support. This work was supported by grant numbers 31630090, 2016YFA0500402, 31422027, 31371118 and 2015CB910102 to B.X.; 31570730, 2016YFA0501102 and 2016YFA0501902 to X.L.; and 21375010 to M.-Q.D., from either the National Natural Science Foundation of China or the National Key R&D Program of China. B.X. and X.L. are awardees of the Young Thousand Talent Program of China.

Author Contributions Q.Z. performed cloning, protein purification, immunostaining and EM data collection; H.Z. performed EM sample preparation, data collection and analysis; S.C., Y.W., J.G., K.W., W.L. and T.Z. carried out biochemical and functional studies; J.W. performed mass spectrometry under the supervision of M.-Q.D.; J.W. built the model; X.L. directed the EM data collection and analysis; B.X. conceived and directed the study, analysed the structure and assisted in model building, made figures and wrote the manuscript with help from all other authors.

Author Information Reprints and permissions information is available at www.nature.com/reprints. The authors declare no competing financial interests. Readers are welcome to comment on the online version of the paper. Publisher's note: Springer Nature remains neutral with regard to jurisdictional claims in published maps and institutional affiliations. Correspondence and requests for materials should be addressed to B.X. (xbailong@mail.tsinghua.edu.cn) or X.L. (lixueming@mail.tsinghua.edu.cn).

Reviewer Information *Nature* thanks E. McCleskey and the other anonymous reviewer(s) for their contribution to the peer review of this work.

METHODS

No statistical methods were used to predetermine sample size. The experiments were not randomized and investigators were not blinded to allocation during experiments and outcome assessment.

Molecular cloning. All constructs were subcloned by using the One Step Cloning Kit (Vazyme Biotech) according to the instruction manual and as described previously³, then sequenced to validate the desired mutations. The loop deletion mutants include Δ L3–4 (84–122), Δ L7–8 (275–317), Δ L11–12 (492–521), Δ L15–16 (657–677), Δ L19–20 (870–921), and Δ L23–24 (1060–1150).

Protein expression and purification. The purification of the mouse Piezo1 protein was performed essentially as in our previously described protocols except for the following two modifications³. First, the time for purification was shortened to within two days. Second, the collection volume of each peak fraction was reduced to obtain more homogeneous fractions. The fresh protein, not subjected to a concentration step, was then directly used for cryo-sample preparation.

Sample preparation and cryo-electron microscopy data acquisition. Aliquots (4 μ l) of detergent-solubilized mouse Piezo1 at a concentration of approximately 0.18 mg ml⁻¹ were applied to glow-discharged 300-mesh Quantifoil R2/2 grids (Quantifoil, Micro Tools GmbH) coated with a homemade continuous thin carbon layer. After a 15-s waiting time, the grids were blotted for 3.5 s and plunged into liquid ethane using an FEI Mark IV Vitrobot operated at 8 °C and 100% humidity. The grids were transferred to a Titan Krios (FEI) electron microscope operating at a voltage of 300 kV with a K2 Summit direct electron detector (Gatan) in the super-resolution counting mode. Data acquisition was performed using UCSF-Image4³⁰ with a nominal magnification of \times 22,500, which yields a super-resolution pixel size of 0.66 Å on image plane, and with defocus ranging from -1.5μ m to -3.0μ m. The dose rate on the detector was approximately 8.2 counts per pixel per second with a frame exposure time of 0.25 s and a total exposure time of 8 s. Each micrograph stack contains 32 frames. The total dose rate was approximately 50 e⁻ Å⁻² for each micrograph.

Image processing. A simplified diagram of the procedure for image processing is presented in Extended Data Fig. 2. A total of 5,840 and 4,331 cryo-EM micrographs from two datasets were manually collected for the mouse Piezo1 proteins. The motion correction was performed using MotionCorr³¹ with 2×2 binning, resulting in a pixel size of 1.32 Å. The output stacks from MotionCorr were further motion corrected with MotionCorr2³², and meanwhile, dose weighting was performed, yielding motion-corrected integrated images for further processing. The whole image defocus parameters were estimated by CTFIND3³³. A total of 1,417,116 and 1,405,683 particles were respectively autopicked from the two batches of the datasets by RELION 1.4³⁴. Several rounds of two-dimensional (2D) classification were then performed. Those particles in the classes with fuzzy class averages were considered as bad particles and excluded from further analysis. Finally, 377,175 and 203,621 particles from the two batches were selected for further three-dimensional (3D) analysis, respectively. A cylinder model generated by SPIDER³⁵ was used as the initial model for the first round of 3D refinement. Then, each particle was re-centred using the in-plane translations measured in 3D refinement and re-extracted from the motion-corrected integrated micrographs. Gctf³⁶ was used to refine the local defocus parameters. The well-centred particles with more accurate defocus parameters were subjected to further 3D refinement, which resulted in two electron density maps at 4.25 Å and 4.86 Å resolution, respectively. The particles from the two datasets were pooled together to expand the data volume. A total of 465,503 particles with clear secondary-structure features in the corresponding class averages were selected after further 2D classification, and subjected to 3D refinement, resulting in a map at 4.15 Å resolution. To further eliminate heterogeneous particles, we used a random-phase 3D classification method³⁷, and the remained 238,529 good particles were subjected to a final 3D refinement. Eventually, the resolution was improved to 3.97 Å.

The particles selected from the random-phase 3D classification were also subjected to 3D classification with C3 symmetry using refined orientations based on the 3.97 Å map, while no image alignment was performed in the 3D classification to limit the uncertainty of the angular search. The particles of the two classes with the largest variations were chosen and subjected to one additional round of 3D auto-refinement, which resulted in two reconstructions with overall resolutions of 4.51 Å and 4.40 Å. To examine whether the three subunits within the trimeric channel might move independently, the 4.15 Å reconstruction was subjected to an additional round of 3D classification without symmetry.

To improve the density of the far end of the blade region, another two replicas of particles with $-120^\circ/120^\circ$ rotation on the pseudo-C3 axis were added to the original particles, and then projections of the cap and the other two blades were subtracted from the tripled experimental particle images. The remaining particles were processed following a focused classification procedure³⁸, which resulted in a blade map at 4.86 Å resolution showing better resolved TM helices. To improve the density of the linker between the termini of the CED and the OH and IH

projections of the peripheral regions of the blades were subtracted from the experimental images, and the remaining particles were processed following a focused classification procedure, which resulted in a pore map at 4.25 Å resolution.

The reported resolutions are based on the gold-standard Fourier shell correlation (FSC) 0.143 criterion³⁹. All density maps were sharpened by applying a negative B-factor that was estimated using automated procedures⁴⁰. Local resolution variations were estimated using Blocres⁴¹.

Model building and structure refinement. The TM regions of mouse Piezo1 in the sequence were predicted by HMMTOP⁴². The crystal structure of CED (PDB accession 4RAX³) was docked into the cryo-EM map in Chimera⁴³. The remaining part of the model was built *de novo* in COOT⁴⁴. The cryo-EM map showed clear side chain features in the C-terminal region, which allowed us to build the atomic model including side chains from residues 972 to the C-terminal 2547, with the remaining TM helices as poly-alanines. The topology of the whole structure was refined using MDFF⁴⁵ and phenix.real_space_refine⁴⁶ with NCS restraints.

Piezo1 cross-linking and LC-MS/MS analysis. The purified Piezo1 proteins were cross-linked at room temperature with DSS (disuccinimidyl suberate), BS3 (bis[sulfosuccinimidyl] suberate), and sulfo-GMBS (*N*-[*g*-maleimidobutyryloxy] sulfosuccinimide ester), the spacer arm lengths of which are 7.3 Å, 11.4 Å and 11.4 Å, respectively. The samples were then digested and subjected to liquid chromatography–tandem mass spectrometry (LC-MS/MS) analysis. The cross-linked peptides were identified using the pLink software as previously described⁴⁷.

Immunostaining. Live-cell labelling was carried out following the procedure reported previously⁴.

Whole-cell electrophysiology and mechanical stimulation. The protocols for HEK293T cell culture, transient transfection and patch-clamp experiments with an Axopatch 200B amplifier (Axon Instruments) or HEKA EPC10 were essentially similar to those previously described⁴. For whole-cell patch-clamp recordings, the recording electrodes had a resistance of 2–3 M Ω when filled with an internal solution composed of (in mM) 133 CsCl, 1 CaCl₂, 1 MgCl₂, 5 EGTA, 10 HEPES (pH 7.3 with CsOH), 4 MgATP and 0.4 Na₂GTP. The extracellular solution was composed of (in mM) 133 NaCl, 3 KCl, 2.5 CaCl₂, 1 MgCl₂, 10 HEPES (pH 7.3 with NaOH) and 10 glucose. All experiments were carried out at room temperature. The currents were sampled at 20 kHz, filtered at 2 kHz using the Clampex 10.4 software (Axon Instruments) or Patchmaster software. Leak currents before mechanical stimulation were subtracted off-line from the current traces.

Mechanical stimulation was delivered to the cell during the patch-clamp recording at an angle of 80° using a fire-polished glass pipette (tip diameter 3–4 μ m) as previously described^{1,2}. The downward movement of the probe towards the cell was driven by a Clampex controlled Piezo-electric crystal micro-stage (E625 LVPZT Controller/Amplifier; Physik Instrument). The probe had a velocity of 1 μ m ms⁻¹ during the downward and upward motion, and the stimulus was maintained for 150 ms. A series of mechanical steps in 1- μ m increments was applied every 20 s, and the currents were recorded at a holding potential of -70 mV. Yoda1 was solubilized in DMSO as a stock solution of 30 mM and diluted to a final concentration of 30 μ M using the extracellular solution. The poking-induced currents were recorded within 10 min using the extracellular solution with or without 30 μ M Yoda1.

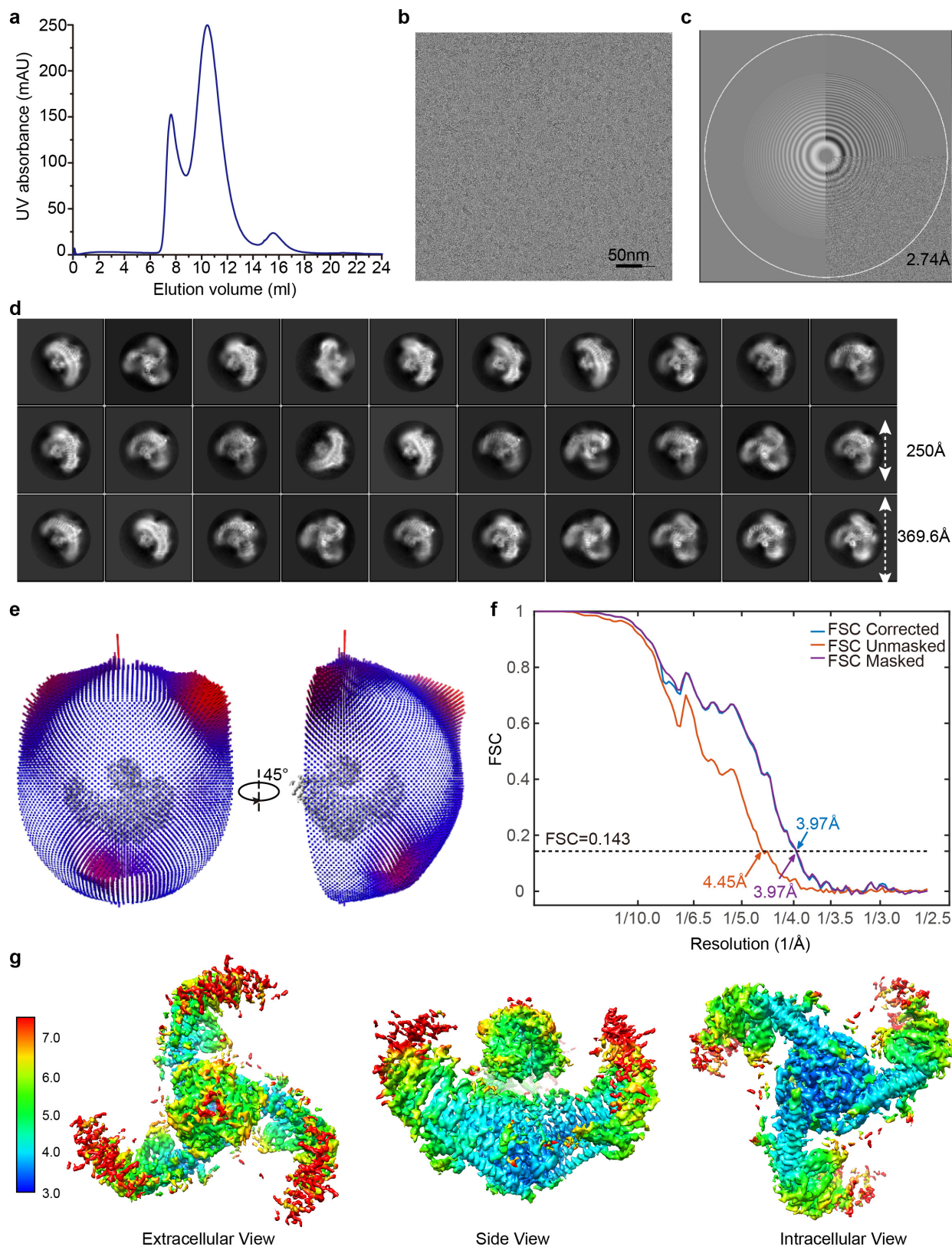
Cell-attached electrophysiology. Stretching-activated currents were recorded in the cell-attached patch-clamp configuration as previously described⁴. The currents were sampled at 20 kHz and filtered at 2 kHz. The pipettes were filled with a solution consisting of (in mM) 130 NaCl, 5 KCl, 10 HEPES, 1 CaCl₂, 1 MgCl₂ and 10 TEA-Cl (pH 7.3, balanced with NaOH). The external solution used to zero the membrane potential consisted of (in mM) 140 KCl, 10 HEPES, 1 MgCl₂ and 10 glucose (pH 7.3 with KOH). All experiments were performed at room temperature. The membrane patches were stimulated with negative pressure pulses for 500 ms through the recording electrode using a Patchmaster controlled pressure clamp HSPC-1 device (ALA-scientific). Stretching-activated channels were recorded at a holding potential of -80 mV with pressure steps from 0 to -100 mm Hg (-10 mm Hg increments), and 4–11 recording traces were averaged per cell for analysis. The current–pressure relationships were fitted with a Boltzmann equation of the form $I(P) = [1 + \exp(-(P - P_{50})/s)]^{-1}$, in which I is the peak of the stretching-activated current at a given pressure, P is the applied patch pressure (in mm Hg), P_{50} is the pressure value that evoked a current value of 50% of I_{max} , and s reflects the current sensitivity to pressure.

FLIPR. Human embryonic kidney 293T (HEK293T) cells were grown in DMEM containing 4.5 mg ml⁻¹ glucose, 10% fetal bovine serum, 1% penicillin/streptomycin. Cells were seeded in 50 μ g ml⁻¹ poly-D-lysine-coated 96-well plates (3×10^4 cells per well) and allowed to grow for approximately 18 h, then co-transfected with a total of 250 ng of cDNA containing Piezo1 or the mutants and the genetically encoded Ca²⁺ indicator, GCAMP6s, using Lipofectamine 2000 (Invitrogen, Life Technology). Two days after transfection, the cells were washed with buffer containing HBSS (1.3 mM Ca²⁺) and 10 mM HEPES (pH 7.2).

The 96-well cell plate with 50 μ l of buffer in each well was then transferred to the FLIPR Tetra (Molecular Device) for recording the GCAMP6s fluorescent signal at a time interval of 1 s using an excitation wavelength of 470–490 nm and an emission wavelength of 515–575 nm. The baseline GCAMP6s fluorescent signal without Yoda1 addition was monitored for 15 s, and then the response to Yoda1 was recorded for 200 s after transferring 50 μ l Yoda1 at twice the final concentrations from a separate compound plate into the cell plate. The Yoda1-induced fluorescent signal change was calculated by subtracting the baseline fluorescent signal from the peak fluorescent signal. For each dose point of Yoda1, the data were averaged from four repetitive wells. The representative traces of the fluorescence signal change of the GCAMP6s in response to 30 μ M Yoda1 are shown in Extended Data Fig. 9i.

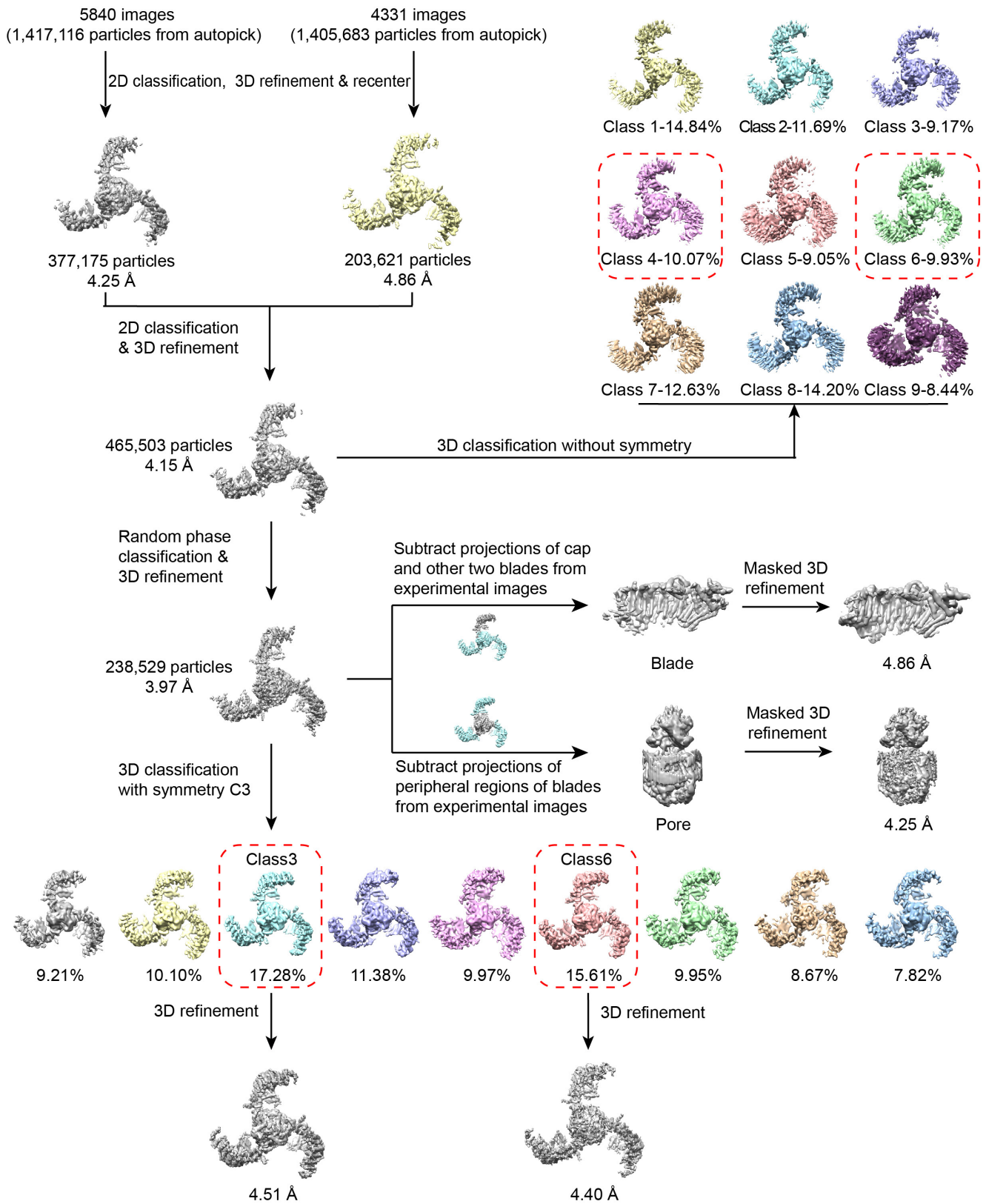
Data availability. The structural coordinates of mouse Piezo1 have been deposited in the Protein Data Bank (PDB) under the accession code 5Z10. The cryo-EM map has been deposited into the Electron Microscopy Data Bank (EMDB) under the accession code EMD-6865. All other data can be obtained from the corresponding authors upon reasonable request.

30. Li, X., Zheng, S., Agard, D. A. & Cheng, Y. Asynchronous data acquisition and on-the-fly analysis of dose fractionated cryoEM images by UCSFImage. *J. Struct. Biol.* **192**, 174–178 (2015).
31. Li, X. *et al.* Electron counting and beam-induced motion correction enable near-atomic-resolution single-particle cryo-EM. *Nat. Methods* **10**, 584–590 (2013).
32. Zheng, S. Q. *et al.* MotionCor2: anisotropic correction of beam-induced motion for improved cryo-electron microscopy. *Nat. Methods* **14**, 331–332 (2017).
33. Mindell, J. A. & Grigorieff, N. Accurate determination of local defocus and specimen tilt in electron microscopy. *J. Struct. Biol.* **142**, 334–347 (2003).
34. Scheres, S. H. RELION: implementation of a Bayesian approach to cryo-EM structure determination. *J. Struct. Biol.* **180**, 519–530 (2012).
35. Shaikh, T. R. *et al.* SPIDER image processing for single-particle reconstruction of biological macromolecules from electron micrographs. *Nat. Protocols* **3**, 1941–1974 (2008).
36. Zhang, K. Gctf: Real-time CTF determination and correction. *J. Struct. Biol.* **193**, 1–12 (2016).
37. Gong, X. *et al.* Structural insights into the Niemann-Pick C1 (NPC1)-mediated cholesterol transfer and Ebola infection. *Cell* **165**, 1467–1478 (2016).
38. Bai, X. C., Rajendra, E., Yang, G., Shi, Y. & Scheres, S. H. Sampling the conformational space of the catalytic subunit of human γ -secretase. *eLife* **4**, e11182 (2015).
39. Scheres, S. H. & Chen, S. Prevention of overfitting in cryo-EM structure determination. *Nat. Methods* **9**, 853–854 (2012).
40. Rosenthal, P. B. & Henderson, R. Optimal determination of particle orientation, absolute hand, and contrast loss in single-particle electron cryomicroscopy. *J. Mol. Biol.* **333**, 721–745 (2003).
41. Cardone, G., Heymann, J. B. & Steven, A. C. One number does not fit all: mapping local variations in resolution in cryo-EM reconstructions. *J. Struct. Biol.* **184**, 226–236 (2013).
42. Tusnady, G. E. & Simon, I. The HMMTOP transmembrane topology prediction server. *Bioinformatics* **17**, 849–850 (2001).
43. Pettersen, E. F. *et al.* UCSF Chimera—a visualization system for exploratory research and analysis. *J. Comput. Chem.* **25**, 1605–1612 (2004).
44. Emsley, P., Lohkamp, B., Scott, W. G. & Cowtan, K. Features and development of Coot. *Acta Crystallogr. D* **66**, 486–501 (2010).
45. Trabuco, L. G., Villa, E., Mitra, K., Frank, J. & Schulten, K. Flexible fitting of atomic structures into electron microscopy maps using molecular dynamics. *Structure* **16**, 673–683 (2008).
46. Adams, P. D. *et al.* PHENIX: a comprehensive Python-based system for macromolecular structure solution. *Acta Crystallogr. D* **66**, 213–221 (2010).
47. Yang, B. *et al.* Identification of cross-linked peptides from complex samples. *Nat. Methods* **9**, 904–906 (2012).

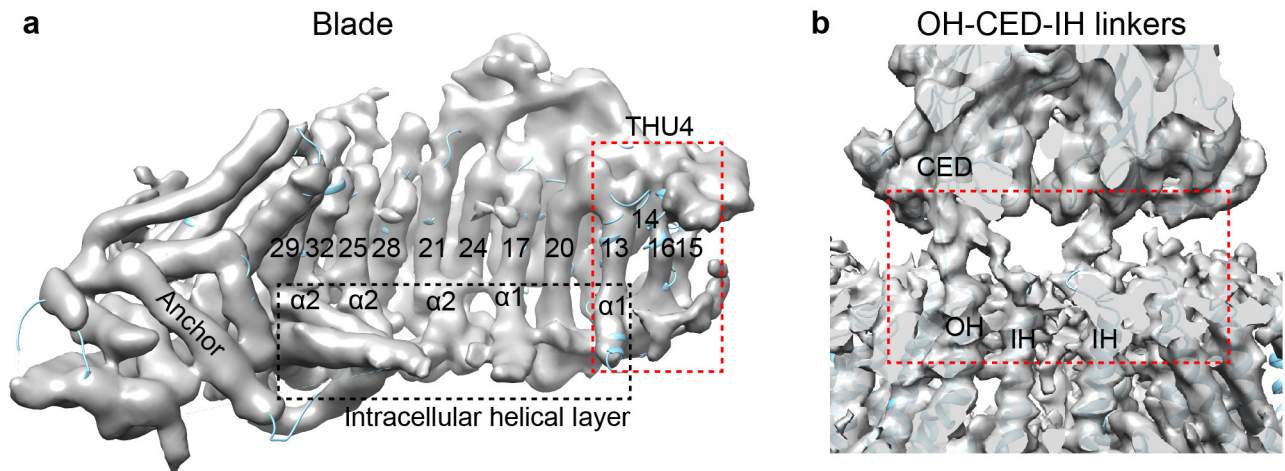


Extended Data Figure 1 | Purification and cryo-EM analysis of Piezo1.
a, A representative trace of gel filtration of the full-length mouse Piezo1. UV, ultraviolet. The experiment was independently repeated more than three times with similar results. **b**, A representative cryo-electron micrograph of Piezo1. The experiment was independently repeated more than three times with similar results. **c**, Power spectrum of the micrograph in **b**, with the 2.74 Å frequency indicated. **d**, Representative 2D class averages of Piezo1 particles. **e**, Euler angle distribution of particles used in the final 3D reconstruction, the height of the cylinder is proportional

to the number of particles for that view. **f**, Gold-standard Fourier shell correlation (FSC) curves of the final density map. The FSC curves were calculated with (purple) or without (red) the application of a soft mask to the two half-set maps. The final FSC curve (blue) was corrected for the soft-mask-induced effect. Reported resolutions were based on the FSC = 0.143 criteria. **g**, The final 3D density map of Piezo1 shown in the indicated views is coloured according to the local resolutions estimated by the software Blocres.

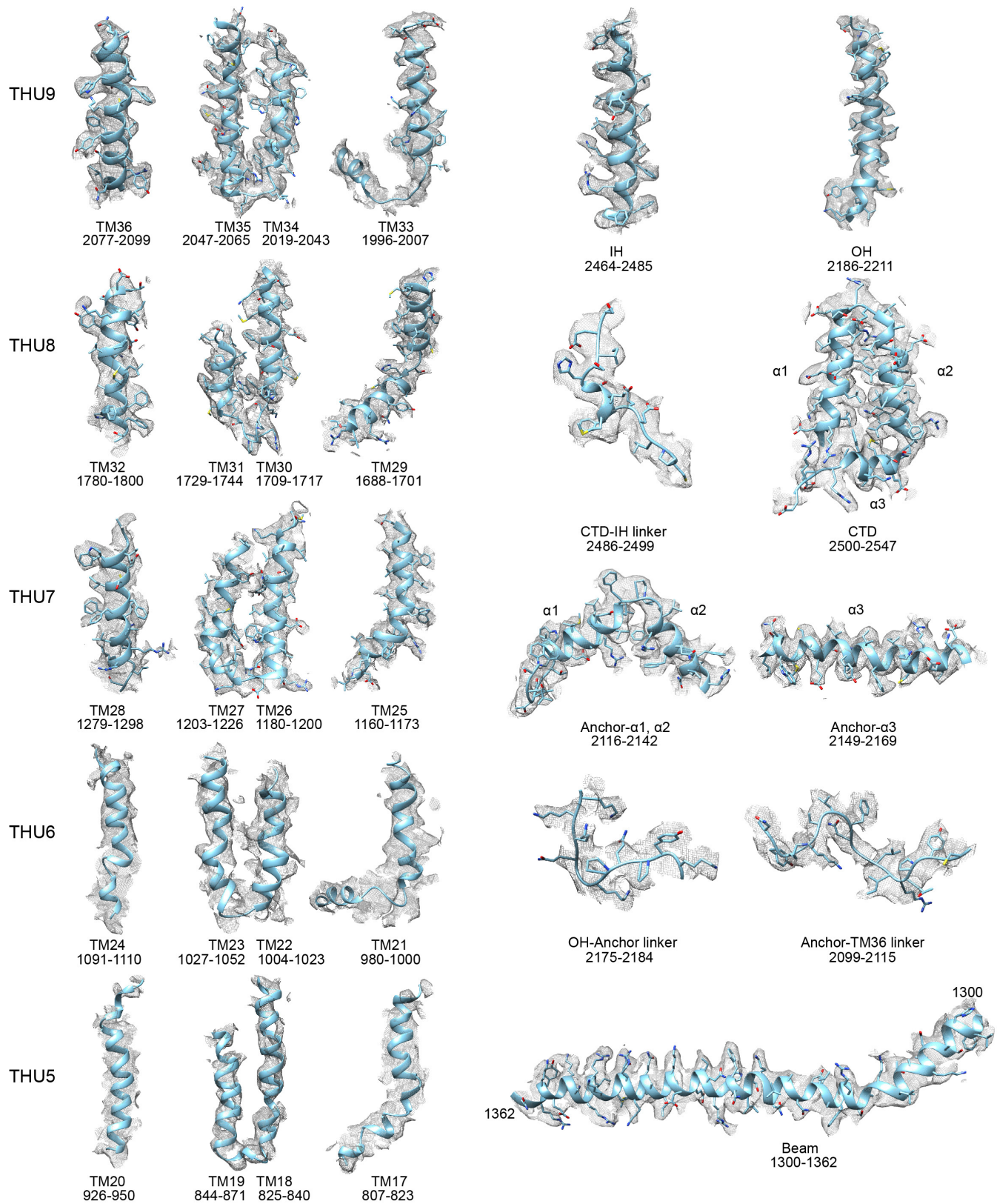


Extended Data Figure 2 | Flowchart of EM data processing. Details of data processing are described in the 'Image processing' section of the Methods.

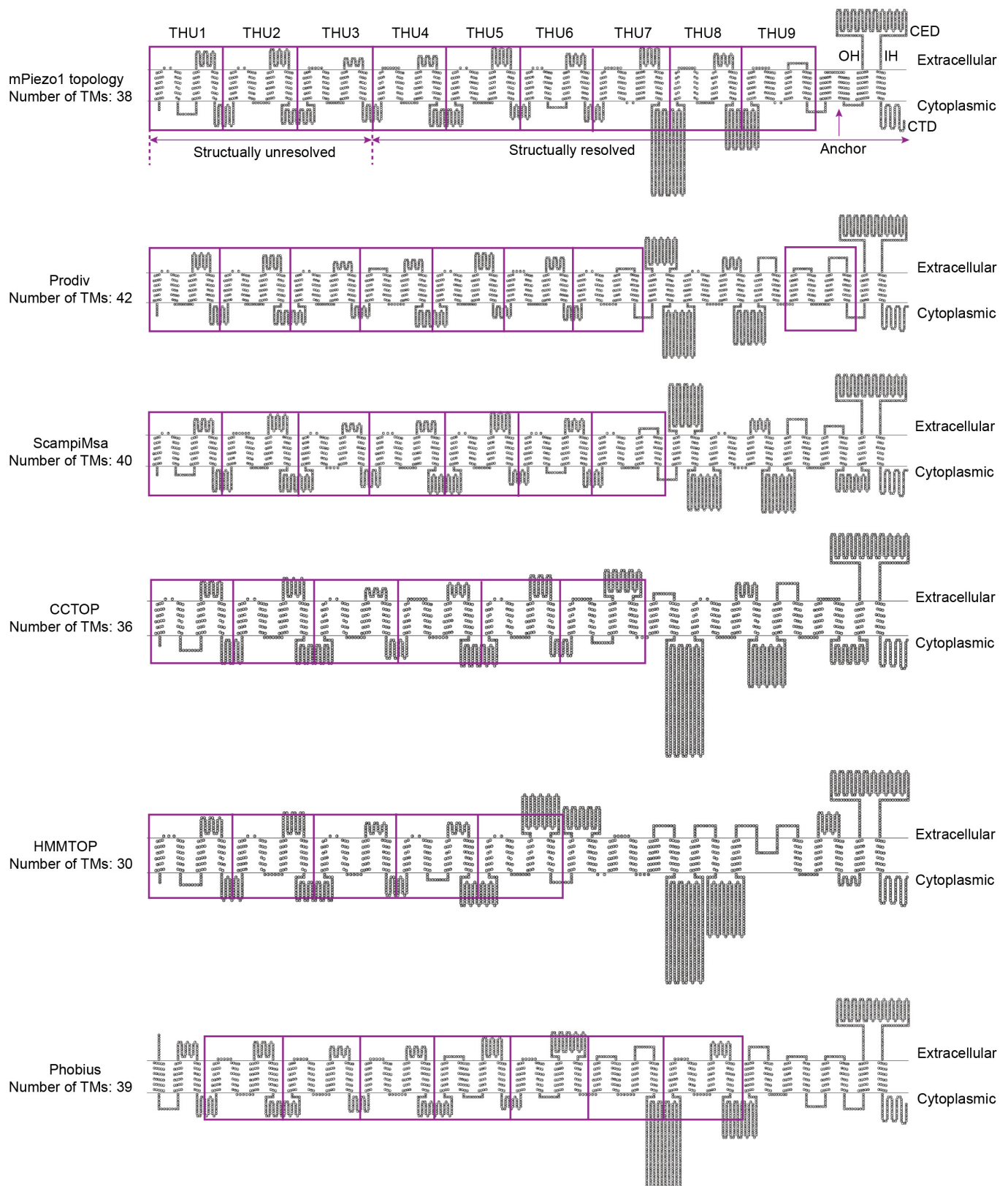


Extended Data Figure 3 | Subtraction of the projection. **a**, Subtraction of the projection of the cap and the other two blades. A distinguishable map of THU4, comprising TM13–TM16, is shown in the red dashed box. Intracellular helical layer, containing several α -helices respectively

connecting to TM29, TM25, TM21, TM17 and TM13, is highlighted in the black dashed box. **b**, Subtraction of the projection of the three blades projection. Identifiable linkers between OH and CED as well as IH and CED are shown in the red dashed box.

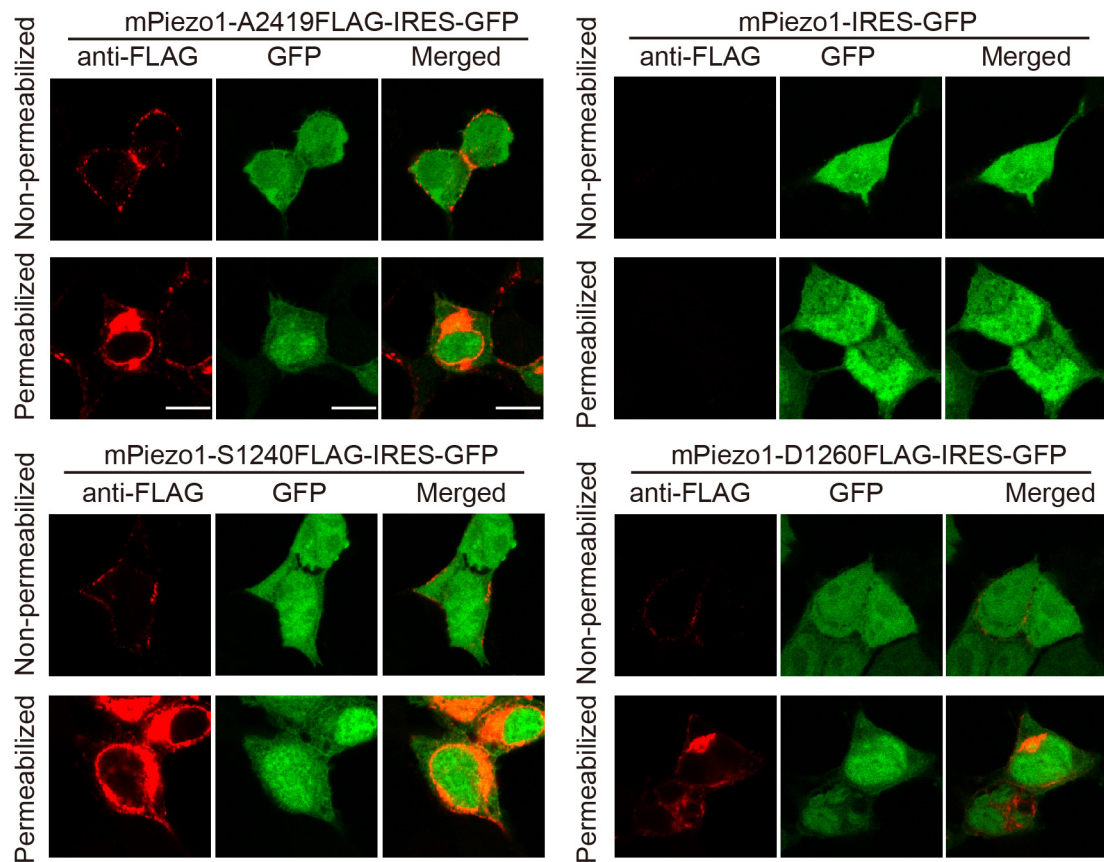


Extended Data Figure 4 | View of the indicated structural domains illustrates the quality of the cryo-EM density of Piezo1. The helices are shown in cartoon representation with side chains as sticks. The cryo-EM density is shown as grey mesh.



Extended Data Figure 5 | Membrane topology of mouse Piezo1. On the basis of various membrane topology prediction algorithms, the N-terminal region contains unanimously predicted THUs (highlighted in the purple boxes) that show typical features of the structurally revealed THU7–

THU9. On the basis of the resolved 3D structure and the predicted THUs, we propose that mouse Piezo1 possesses a 38-TM topology comprising 9 tandem THUs and the OH and IH (top panel). Diagrams were drawn using the TOPO2 program.



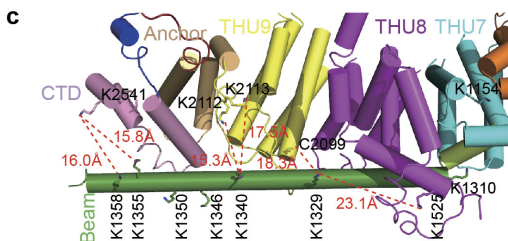
Extended Data Figure 6 | The TM27–TM28 loop containing the S1240 and D1260 residues is located at the extracellular side. Immunofluorescent staining images of cells transfected with the indicated constructs using the anti-Flag antibody either in live-labelling (top) or

after fixation and permeabilization (bottom). Scale bars, 10 μm . GFP, green fluorescent protein; IRES, internal ribozyme entry site. The experiments were repeated in two coverslips with similar results.

a

BS ³ /DSS (K-K)	Site 1	Site2	#Spec-Total	Best E-value		
THU8-9	TM32-33	- 145	TM4-5	THU1-2	2	4.9E-05
		- 1815	TM32-33	THU8-9	10	1.5E-08
		- 1879			9	9.7E-08
		- 1815			3	1.2E-05
		- 1823			76	2.2E-09
		- 1862	TM32-33	THU8-9	8	3.8E-08
		- 1879			3	2.7E-05
		- 1969			8	5.0E-07
		- 1828	TM32-33	THU8-9	9	1.1E-10
		- 349	TM8-9	THU2-3	1	1.6E-05
		- 1372	TM28-29	THU7-8	3	1.8E-05
		- 1815			17	6.2E-11
		- 1828			5	8.4E-06
		- 1834			20	2.6E-07
		- 1862			157	2.0E-14
		- 1868	TM32-33	THU8-9	48	4.1E-12
		- 1879			19	7.9E-07
		- 1894			8	5.3E-10
		- 1921			1	3.0E-05
		- 1937			4	1.4E-08
		- 1969			1	3.7E-06
		- 414	TM8-9	THU2-3	10	8.6E-08
		- 1372	TM28-29	THU7-8	7	1.3E-08
		- 1815			17	2.3E-09
		- 1823			4	3.9E-06
		- 1828			19	3.5E-07
		- 1879	TM32-33	THU8-9	16	4.9E-07
		- 1894			11	2.2E-12
		- 1921			13	1.1E-06
		- 1929			7	3.2E-09
		- 1937			16	1.4E-07
		- 1969			15	5.3E-11
		- 1862	TM32-33	THU8-9	89	1.5E-12
		- 1894			1	3.1E-05
		- 1921			1	6.9E-06
		- 1937			2	8.3E-06
		- 414	TM8-9	THU2-3	1	4.5E-08
		- 1862	TM32-33	THU8-9	9	6.6E-06
		- 1894			34	1.6E-09
		- 1937			1	7.9E-05
		- 1815			3	1.8E-07
		- 1823			1	5.6E-05
		- 1879	TM32-33	THU8-9	9	2.2E-11
		- 1921			10	2.7E-07
		- 1929			1	4.0E-06
		- 1937			6	3.5E-07
		- 145	TM4-5	THU1-2	1	1.7E-05
		- 1862			1	1.5E-05
		- 1879			13	4.4E-07
		- 1894	TM32-33	THU8-9	35	2.9E-10
		- 1900			1	7.1E-05
		- 1921			17	1.5E-06
		- 1937			4	4.7E-07
		- 145	TM4-5	THU1-2	1	3.8E-05
		- 1921	TM32-33	THU8-9	81	1.2E-09
		- 1937			89	4.1E-15
		- 414	TM8-9	THU2-3	8	1.1E-09
		- 1879	TM32-33	THU8-9	13	4.0E-07
		- 1921			39	3.8E-10
		- 1931			39	1.6E-06
		- 414	TM8-9	THU2-3	6	5.3E-08
		- 1815			27	2.0E-12
		- 1879	TM32-33	THU8-9	13	7.9E-08
		- 1937			3	8.5E-06

BS ³ /DSS (K-K)	Site 1	Site2	#Spec-Total	Best E-value		
Beam		- 145	TM4-5	THU1-2	1	1.7E-06
		- 775	TM16-17	THU4-5	2	4.2E-07
		- 1525	TM28-29	THU7-8	10	2.9E-10
		- 1862			7	1.4E-16
		- 1879	TM32-33	THU8-9	3	1.5E-06
		- 1969			10	3.1E-11
		- 1154	TM24-25	THU6-7	1	3.1E-05
		- 1310			19	5.2E-11
		- 1340	TM28-29	THU7-8	9	1.2E-09
		- 1525			32	3.0E-10
		- 1815			6	4.4E-08
		- 1862			16	7.3E-09
		- 1879	TM32-33	THU8-9	1	8.7E-05
		- 1894			1	5.1E-06
		- 1969			6	1.5E-07
		- 1525	TM28-29	THU7-8	4	9.1E-06
		- 1823	TM32-33	THU8-9	2	4.6E-05
		- 1862			6	3.8E-09
		- 2112			25	5.6E-09
		- 2113			6	5.2E-09
		- 186	TM4-5	THU1-2	1	6.0E-06
		- 349	TM8-9	THU2-3	6	1.5E-07
		- 1350	TM28-29	THU7-8	16	4.6E-06
		- 1815			3	5.6E-06
		- 1823			2	1.5E-05
		- 1828			1	7.4E-05
		- 1862	TM32-33	THU8-9	7	1.1E-05
		- 1879			17	8.0E-07
		- 1937			1	5.0E-06
		- 1969			12	3.7E-08
		- 2541	TM38-C	CTD	1	2.9E-07
		- 1879	TM32-33	THU8-9	7	6.1E-08
		- 1847			1	4.2E-05
		- 1862	TM32-33	THU8-9	1	1.7E-05
		- 2541	TM38-C	CTD	2	4.0E-05
		- 1350	TM28-29	THU7-8	5	7.4E-06
		- 1372			8	3.3E-09
		- 1862	TM32-33	THU8-9	3	7.0E-10
		- 2541	TM38-C	CTD	1	2.6E-06
		- 414	TM8-9	THU2-3	11	2.1E-08
		- 1921	TM32-33	THU8-9	3	3.8E-06
		- 1937			3	2.3E-05
		- 145	TM4-5	THU1-2	7	5.3E-08
		- 414	TM8-9	THU2-3	8	9.8E-06
		- 1815	TM32-33	THU8-9	1	6.0E-06
		- 1937			10	5.1E-09
		- 145	TM4-5	THU1-2	10	1.5E-05
		- 349	TM8-9	THU2-3	7	2.3E-08
		- 414			2	2.5E-05
		- 1879			11	4.9E-09
		- 1921	TM32-33	THU8-9	6	2.0E-08
		- 1937			18	1.0E-09
		- 145	TM4-5	THU1-2	4	9.0E-06
		- 414	TM8-9	THU2-3	3	9.6E-10
		- 1937	TM32-33	THU8-9	4	2.4E-07
		- 145	TM4-5	THU1-2	19	4.6E-13
		- 186			17	1.2E-10
		- 349	TM8-9	THU2-3	4	2.4E-09
		- 414			5	1.9E-06
		- 1862	TM32-33	THU8-9	12	4.8E-07
		- 1937			9	7.2E-09
		- 1372	TM28-29	THU7-8	3	9.6E-06
		- 1525			1	3.5E-05
		- 2112	- 2174	TM36-37	6	3.2E-07
		- 2113	- 2174	TM36-37	44	1.3E-11
		- 2388			38	4.7E-16
		- 2438	TM37-38	CTD	2	4.5E-06
		- 2329			3	1.4E-06
		- 2374	TM37-38	CTD	43	3.7E-16
		- 2505	- 2112	TM36-37	2	1.2E-08
		- 1372	TM28-29	THU7-8	8	2.6E-10
		- 1862	TM32-33	THU8-9	5	5.1E-14
		- 1879			4	7.6E-08

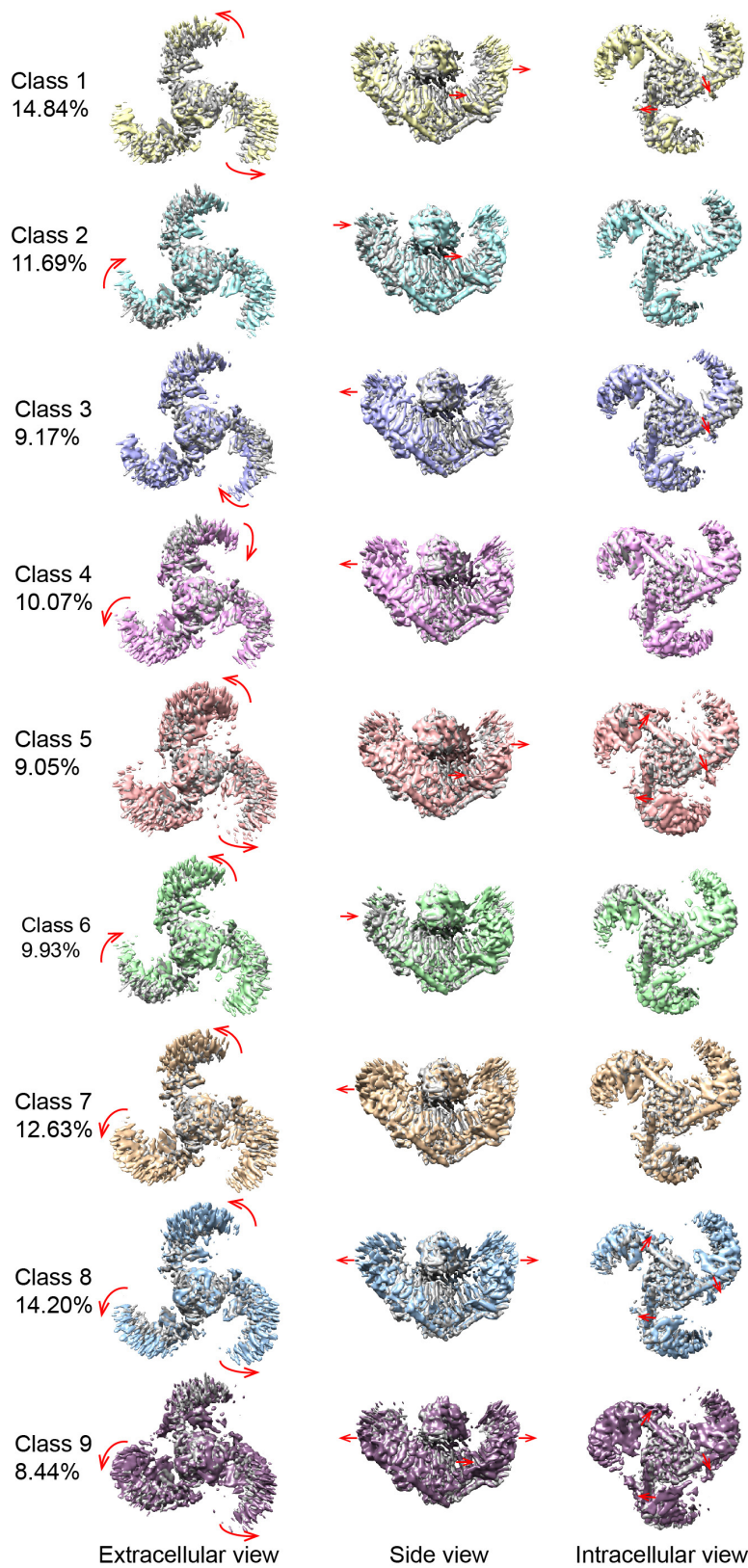


b

sulfo-GMBS (K-C)	Site 1	Site2	#Spec-Total	Best E-value		
THU2-3	TM8-9	349	- 343	THU2-3	1	3.9E-06
THU7-8	Beam	1329	- 2099		65	5.5E-10
	TM28-29	1525	- 2099		3	3.9E-05
THU8-9	TM32-33	1823	- 2099	TM36-37	6	5.6E-10
		1862	- 2099		12	5.3E-07
		1969	- 2099		128	3.4E-13
		1969	- 1818	TM32-33	THU8-9	8
TM36-37	2112	- 2099	TM36-37	24	1.5E-06	

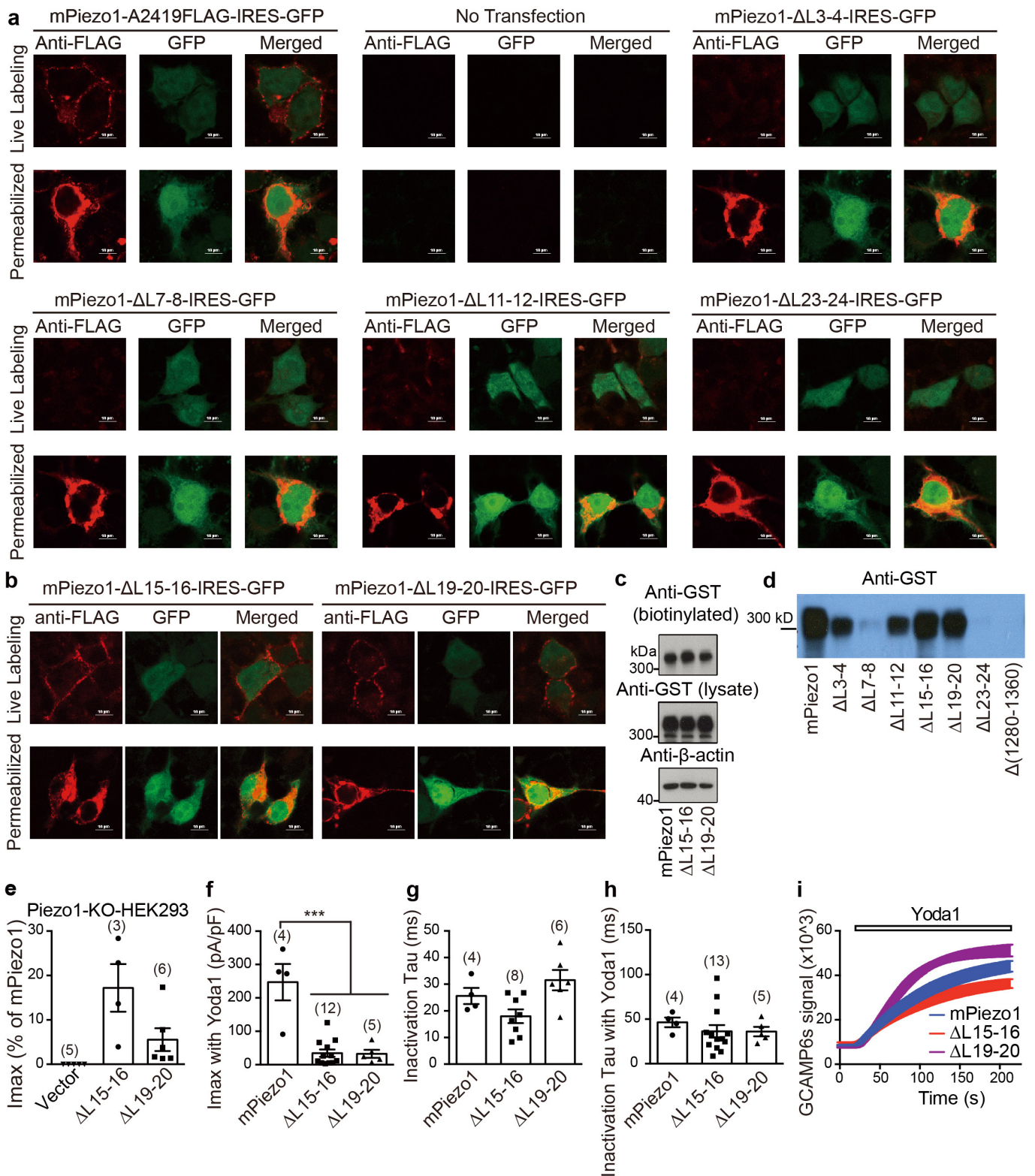
Extended Data Figure 7 | Chemically cross-linked lysine-lysine and lysine-cysteine pairs identified in mouse Piezo1. **a, b,** Purified mouse Piezo1 proteins were cross-linked with BS³/DSS (**a**) or sulfo-GMBS (**b**), and then digested with trypsin. Following LC-MS/MS analysis of the

peptides, cross-linked lysine pairs were identified using pLink. **c,** The diagram shows the cross-linked lysine pairs between residues located in the beam and other regions. The atom-to-atom distance of the cross-linked residues is shown.



Extended Data Figure 8 | Conformational heterogeneity of Piezo1. Nine classes of Piezo1 structures resulting from symmetry-free 3D classification. Conformational heterogeneity is shown by comparing

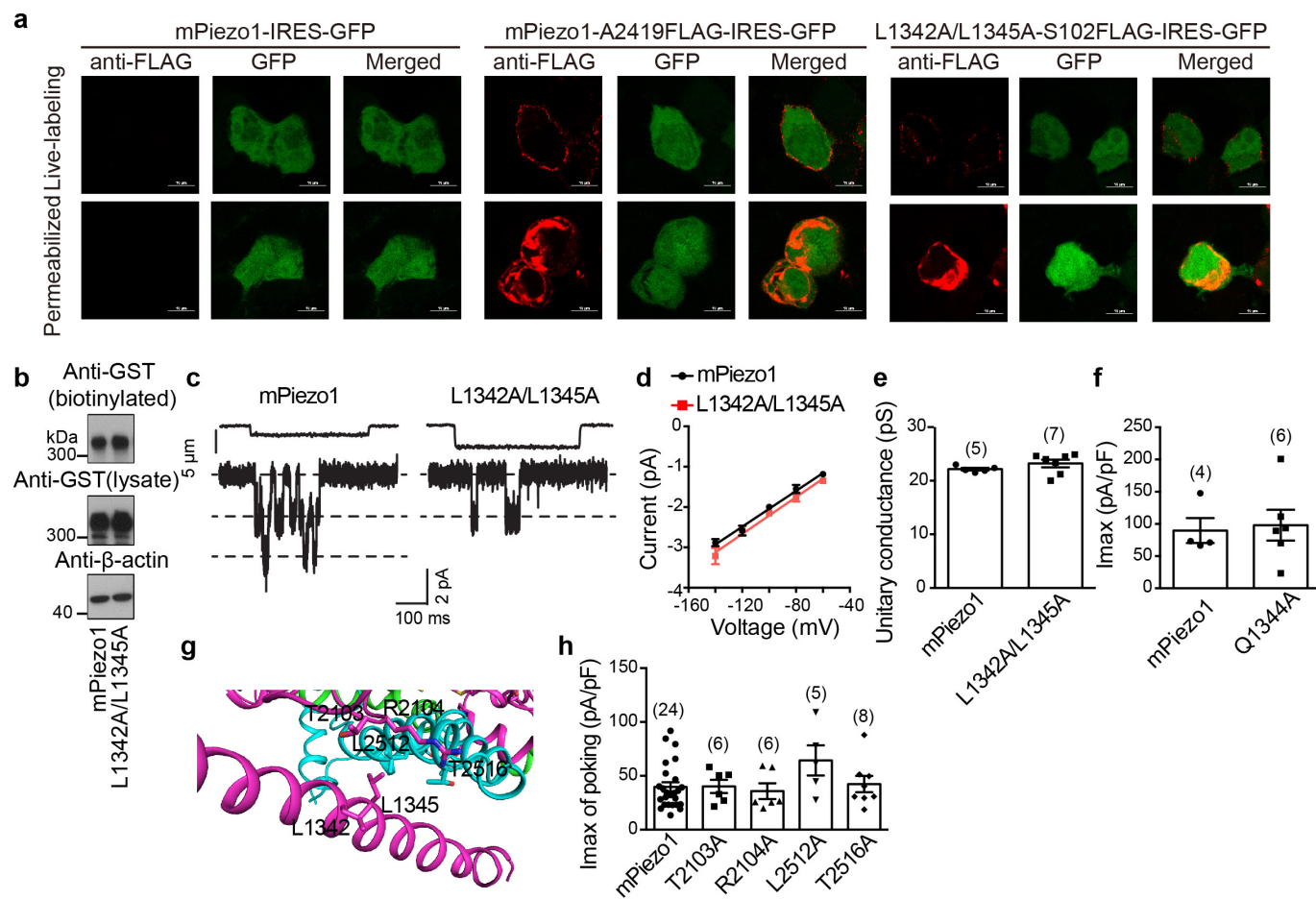
different classes with the low-passed 6 Å map of the 3.97 Å map with C3 symmetry. Red arrows represent the relative movements of the blades and beams.



Extended Data Figure 9 | See next page for caption.

Extended Data Figure 9 | Characterization of the Piezo1 deletion mutants. **a, b**, Immunofluorescent staining images of cells transfected with the indicated constructs using the anti-Flag antibody either in live-labelling (top) or after fixation and permeabilization (bottom). Scale bars, 10 μm . The experiments were repeated in two coverslips with similar results. **c**, Cell surface biotinylation assay showing comparable plasma membrane expression of the indicated constructs. The experiment was independently repeated for two times with similar results. **d**, The glutathione *S*-transferase (GST)-tagged proteins were pulled-down by glutathione beads, followed with western blotting using the anti-GST antibody. The experiment was independently repeated twice with similar results. **e**, Scatter plot of the maximal poking-induced currents of Piezo1-knockout HEK293 cells transfected with the indicated mutants, which were normalized to the mouse Piezo1 current. **f**, Scatter plot of the

maximal poking-induced currents of HEK293T cells transfected with the indicated constructs in the presence of 30 μM Yoda1. *** $P < 0.0001$, one-way ANOVA with Dunn's multiple comparison test. **g, h**, Scatter plot of the inactivation tau of HEK293T cells transfected with the indicated constructs in the absence (**g**) or presence (**h**) of 30 μM Yoda1. In **g**, $P = 0.2267$ and 0.4177 (for $\Delta\text{L15-16}$ and $\Delta\text{L19-20}$, respectively) and in **h**, $P = 0.6263$ and 0.6934 (for $\Delta\text{L15-16}$ and $\Delta\text{L19-20}$, respectively); one-way ANOVA with Dunn's multiple comparison test (compared with Piezo1). **i**, Representative traces of the fluorescence signal change of the genetically encoded Ca^{2+} indicator, GCAMP6s, from HEK293T cells co-transfected with the indicated constructs and GCAMP6s, in response to 30 μM Yoda1. The experiment was independently repeated three times with similar results. Data in **e-h** are mean \pm s.e.m., and the numbers of recorded cells are indicated above the bars.



Extended Data Figure 10 | Characterization of the L1342A/L1345A mutant. **a**, Immunofluorescent staining images with the anti-Flag antibody either in live-labelling (top) or after fixation and permeabilization (bottom). The experiment was independently repeated three times with similar results. **b**, Cell-surface biotinylation assay showing comparable plasma membrane expression of the indicated constructs. The experiment was independently repeated twice with similar results. **c**, Representative single-channel current traces of the indicated constructs recorded at -140 mV. **d**, Linear regression fit of average I - V relationships of single-channel recordings of the indicated constructs. The number of recorded cells for Piezo1 and the L1342A/L1345A mutant is 5 and 7,

respectively. **e**, Scatter plot of the unitary conductance calculated from fit of individual recordings. $P = 0.2541$, unpaired, two tailed Student's t -test. **f**, Scatter plot of the I_{\max} of poking-induced currents. $P = 0.8076$, unpaired, two tailed Student's t -test. **g**, Structural representation of the L1342 and L1345 residues and those residues in close proximity. **h**, Scatter plot of the I_{\max} of poking-induced currents of cells transfected with the indicated mutants. $P = 0.9976, 0.9281, 0.3804$ and 0.9997 for T2103A, R2104A, L2512A and T2516A, respectively; one-way ANOVA with Dunn's multiple comparison test. Data in **d-f** and **h** are mean \pm s.e.m., and the numbers of recorded cells in **e** and **h** are indicated above the bars.

Life Sciences Reporting Summary

Nature Research wishes to improve the reproducibility of the work that we publish. This form is intended for publication with all accepted life science papers and provides structure for consistency and transparency in reporting. Every life science submission will use this form; some list items might not apply to an individual manuscript, but all fields must be completed for clarity.

For further information on the points included in this form, see [Reporting Life Sciences Research](#). For further information on Nature Research policies, including our [data availability policy](#), see [Authors & Referees](#) and the [Editorial Policy Checklist](#).

Please do not complete any field with "not applicable" or n/a. Refer to the help text for what text to use if an item is not relevant to your study. For final submission: please carefully check your responses for accuracy; you will not be able to make changes later.

▶ Experimental design

1. Sample size

Describe how sample size was determined.

For all functional experiments, the sample sizes represent the number of cells used for experiments and data analysis. And the sample size is determined based on the consistence of the recordings.

2. Data exclusions

Describe any data exclusions.

No data was excluded in patch clamp recordings.

3. Replication

Describe the measures taken to verify the reproducibility of the experimental findings.

All experimental findings were reliably reproduced.

4. Randomization

Describe how samples/organisms/participants were allocated into experimental groups.

For structure refinement and model validation, all particles were randomly split into two groups, one for refinement and the other for validation. For functional experiments, cells with fluorescence were randomly selected for recording or imaging.

5. Blinding

Describe whether the investigators were blinded to group allocation during data collection and/or analysis.

The investigators were blinded to group allocation during data collection and analysis.

Note: all in vivo studies must report how sample size was determined and whether blinding and randomization were used.

6. Statistical parameters

For all figures and tables that use statistical methods, confirm that the following items are present in relevant figure legends (or in the Methods section if additional space is needed).

- | n/a | Confirmed |
|-------------------------------------|--|
| <input type="checkbox"/> | <input checked="" type="checkbox"/> The <u>exact sample size</u> (<i>n</i>) for each experimental group/condition, given as a discrete number and unit of measurement (animals, litters, cultures, etc.) |
| <input type="checkbox"/> | <input checked="" type="checkbox"/> A description of how samples were collected, noting whether measurements were taken from distinct samples or whether the same sample was measured repeatedly |
| <input type="checkbox"/> | <input checked="" type="checkbox"/> A statement indicating how many times each experiment was replicated |
| <input type="checkbox"/> | <input checked="" type="checkbox"/> The statistical test(s) used and whether they are one- or two-sided
<i>Only common tests should be described solely by name; describe more complex techniques in the Methods section.</i> |
| <input checked="" type="checkbox"/> | <input type="checkbox"/> A description of any assumptions or corrections, such as an adjustment for multiple comparisons |
| <input type="checkbox"/> | <input checked="" type="checkbox"/> Test values indicating whether an effect is present
<i>Provide confidence intervals or give results of significance tests (e.g. P values) as exact values whenever appropriate and with effect sizes noted.</i> |
| <input type="checkbox"/> | <input checked="" type="checkbox"/> A clear description of statistics including <u>central tendency</u> (e.g. median, mean) and <u>variation</u> (e.g. standard deviation, interquartile range) |
| <input type="checkbox"/> | <input checked="" type="checkbox"/> Clearly defined error bars in <u>all</u> relevant figure captions (with explicit mention of central tendency and variation) |

See the web collection on [statistics for biologists](#) for further resources and guidance.

► Software

Policy information about [availability of computer code](#)

7. Software

Describe the software used to analyze the data in this study.

RELION 1.4, Coot, ResMap, PHENIX, HOLE, PyMol, Chimera, MotionCorr1, MotionCorr2, pLink, Clampex 10.4, GraphPad Prism 6, CTFIND3, SPIDER, Gctf, MDFF, Phenix, Nikon NIS-Elements AR software

For manuscripts utilizing custom algorithms or software that are central to the paper but not yet described in the published literature, software must be made available to editors and reviewers upon request. We strongly encourage code deposition in a community repository (e.g. GitHub). *Nature Methods* [guidance for providing algorithms and software for publication](#) provides further information on this topic.

► Materials and reagents

Policy information about [availability of materials](#)

8. Materials availability

Indicate whether there are restrictions on availability of unique materials or if these materials are only available for distribution by a third party.

There are no restrictions.

9. Antibodies

Describe the antibodies used and how they were validated for use in the system under study (i.e. assay and species).

anti-FLAG antibody (1:100, Sigma, Cat#: F3165), Alexa Fluor 594 donkey-anti-mouse IgG secondary antibody (1:200, Thermo, Cat#:R37115), rabbit anti-GST (Millipore, 1:3,000) anti- β -actin (Cell Signaling Technology, 1:3,000), peroxidase-conjugated anti-rabbit IgG secondary antibody (CST, 1:10,000) or antimouse IgG secondary antibody (pierce, 1:20,000).

10. Eukaryotic cell lines

a. State the source of each eukaryotic cell line used.

HEK293T, P1-KO-HEK293 cell line

b. Describe the method of cell line authentication used.

HEK293T was from ATCC, P1-KO-HEK293 cell line was from Ardem Patapoutian lab, which was validated as mentioned in Lukacs 2015(PMID:2638713).

c. Report whether the cell lines were tested for mycoplasma contamination.

Test negative.

d. If any of the cell lines used are listed in the database of commonly misidentified cell lines maintained by [ICLAC](#), provide a scientific rationale for their use.

No commonly misidentified cell lines were used.

► Animals and human research participants

Policy information about [studies involving animals](#); when reporting animal research, follow the [ARRIVE guidelines](#)

11. Description of research animals

Provide all relevant details on animals and/or animal-derived materials used in the study.

No animals were used in the study.

Policy information about [studies involving human research participants](#)

12. Description of human research participants

Describe the covariate-relevant population characteristics of the human research participants.

No human research participants were used in the study.

CORRECTIONS & AMENDMENTS

CORRECTION

<https://doi.org/10.1038/s41586-018-0513-4>

Author Correction: Structure and mechanogating mechanism of the Piezo1 channel

Qiancheng Zhao, Heng Zhou, Shaopeng Chi, Yanfeng Wang, Jianhua Wang, Jie Geng, Kun Wu, Wenhao Liu, Tingxin Zhang, Meng-Qiu Dong, Jiawei Wang, Xueming Li & Bailong Xiao

Correction to: *Nature* <https://doi.org/10.1038/nature25743>, published online 22 January 2018.

In Extended Data Fig. 9a of this Article, the bottom photomicrographs (labelled 'permeabilized') of mPiezo1- Δ L3-4-IRES-GFP and mPiezo1- Δ L7-8-IRES-GFP were inadvertently duplicated, after the wrong photomicrographs were inserted for mPiezo1- Δ L7-8-IRES-GFP. The correct figure panels are shown below as Fig. 1, and the original Article has not been corrected. We thank the reader who pointed out this error.

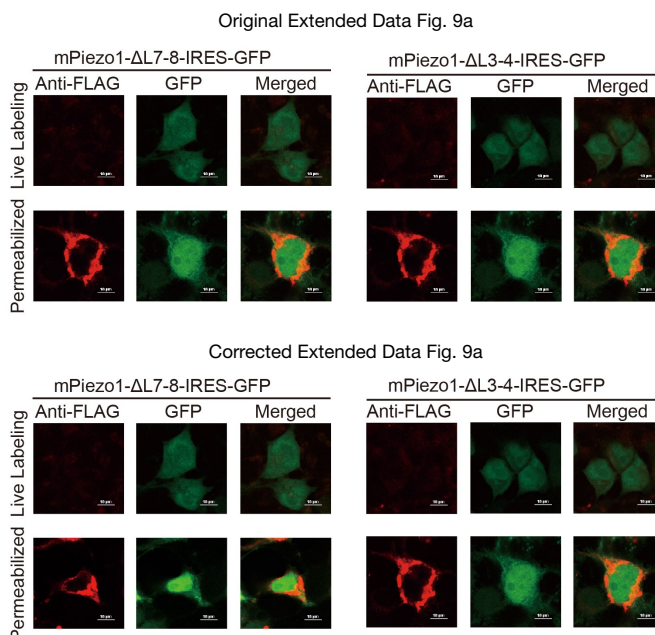


Fig. 1 | This figure shows the original and the corrected panels from Extended Data Fig. 9a of the original Article.